Creation of Error Signals for Frequency-stabilizing a Grating Laser to Rubidium Transitions Using Modulation Transfer Spectroscopy

Bennet Sohn

Bachelorarbeit in Physik
angefertigt im Institut für Angewandte Physik (IAP)
vorgelegt der
Mathematisch-Naturwissenschaftlichen Fakultät
der
Rheinischen Friedrich-Wilhelms-Universität
Bonn

März 2024

Ich versichere, dass ich diese Arbeit selbstständig verfasst und keine anderen als die angegebenen Quellen und Hilfsmittel benutzt sowie die Zitate kenntlich gemacht habe.

Bonn, 04.03.2024 ..... Bawet Sder .....

Datum Unterschrift

1. Gutachter: Prof. Dr. Sebastian Hofferberth
2. Gutachter: Dr. Frank Vewinger

Contents

CHAPTER 1

Introduction

Frequency stabilized lasers have copious amounts of applications. They can be used for laser trapping and cooling [1] and high resolution spectroscopy [2]. An important case is reliable excitation of atoms [3]. Narrow linewidth lasers allow to address different atomic hyperfine states. Since their transition frequencies are typically very similar, they are hard to resolve. Apart from that, narrow linewidth lasers also allow to excite atomic Rydberg-states, which is usually rendered difficult due to the small linewidth of Rydberg-states.

Rubidium is a very popular choice of element to work with in Rydberg-experiments. It belongs to the group of the alkali metals (first group in the periodic table) and therefore has only one valence electron rendering the energy level scheme relatively simple (to calculate and predict). The excitation energies correspond to light frequencies that are commonly available with a number of commercial lasers. It also is a comparably cheap and readily available alkali metal making it a very practical choice for Rydberg-experiments.

The spectroscopy of Rubidium plays a vital role in the work of this thesis. The goal is to resolve hyperfine states of $6P_{3/2}$ in the Rubidium spectrum. They function as references to which a laser will be stabilized. This, however, poses a number of challenges, such as the low absorption of laser light at room temperature and the fact that the hyperfine states are very close to each other on a frequency scale. A heated Rubidium vapor cell and a spectroscopy setup insensitive to Doppler-broadening solves these issues.

There are a number of different methods for frequency-stabilization of lasers. They include polarization spectroscopy [2] [4], frequency modulation spectroscopy [5] and modulation transfer spectroscopy (MTS) [6]. The last of which will be used in this experiment because it gives an offset-free error signal. The aim of MTS is to utilize an electro-optical modulator (EOM) to periodically modulate the phase of a laser beam, which in turn transfers its modulation to a second counter propagating beam. With this beam an error signal is created which can then be employed to frequency stabilize the laser.

Ultimately the frequency stabilized laser will be implemented to drive the $5S_{1/2} \rightarrow 6P_{3/2}$ transition in Rubidium 87 in another experiment allowing the excitation of Rydberg-atoms in a so called *inverted excitation scheme*. This scheme was for example used in photon storage experiments. For more detail see [7].

Chapter 2 deals with the spectroscopy of Rubidium, explaining the level scheme (sec. 2.1), the high temperature spectroscopy cell setup (sec. 2.2), discussing the methods of absorption spectroscopy (sec. 2.3) and saturated absorption spectroscopy (sec. 2.4) and evaluating the measured data respectively.

Chapter 3 then goes on to discuss the theoretical background of EOMs and MTS (sec. 3.1). The experimental setup including the EOM and its resonance circuit is explained in section 3.2. Section 3.3 evaluates and discusses the measured data on achieved phase modulation and creation of error signals.

CHAPTER 2

Spectroscopy of $6P_{3/2}$ Manifold in Rubidium

The spectroscopy of Rubidium plays a vital role in this experiment, since it is the reference against which the laser is frequency-stabilized (see chapter 3). Understanding the level scheme of Rubidium is crucial to be able to work with it. The only stable[1] natural Rubidium isotopes are Rb^{85} and Rb^{87} with 72.17(2)% being Rb^{85} and the remaining 27.83(2)% being Rb^{87} [9].

The aim of this chapter is to resolve hyperfine splitting of the $6P_{3/2}$ state for use in MTS. In section 2.1 of this chapter the energy level scheme of Rubidium is discussed. Section 2.2 deals with the high-temperature spectroscopy cell. In section 2.3 absorption spectroscopy is covered. Section 2.4 expands the topic of absorption spectroscopy to saturated absorption spectroscopy to resolve hyperfine splitting of (excited) energy levels.

2.1 Rb^{85} and Rb^{87} Energy Level Scheme

Considering the ultimate application, only the $5S_{1/2}$ and $6P_{3/2}$ levels[2] will be regarded. The level scheme can be seen in figure 2.1. The transition frequencies of the $5S_{1/2} \rightarrow 6P_{3/2}$ transition for both Rb^{85} and Rb^{87} correspond to a wavelength of approximately 420 nm.

The nuclear spins of the Rubidium isotopes are $I_{Rb^{85}} = 5/2$ and $I_{Rb^{87}} = 3/2$ [11]. It is known that $\vec{F} = \vec{J} + \vec{I}$, hence $F = 2, 3$ for the $5S_{1/2}$ state of Rb^{85} and $F = 1, 2$ for the $5S_{1/2}$ state of Rb^{87}. Taking into account the selection rule for electric dipole transitions $\Delta J = 0, \pm 1 (0 \nleftrightarrow 0)$ [12] and the fact that the nuclear spin $\vec{I}$ is fixed and not affected by transitioning, one can deduce that $\Delta F = 0, \pm 1 (0 \nleftrightarrow 0)$. Subsequently, F for Rb^{87} is $F(6P_{3/2}) = 0, 1, 2, 3$ and for Rb^{85} $F(6P_{3/2}) = 1, 2, 3, 4$. In table 2.2 the possible transitions can be seen.

For excitation the *DL PRO 420* is used. It operates at around 713.8 THz $\approxeq$ 420 nm and can be frequency-tuned by up to several 10 GHz. The stabilized laser will be used to reliably excite the Rb^{87} $5S_{1/2}$ to $6P_{3/2}$ transition in another experiment.

[1] Rb^{87} is actually not entirely stable, but considering its lifetime of 4.88×10^{10} years [8] it can be considered as sufficiently stable.

[2] As a reminder this notation follows the scheme of nL_J.

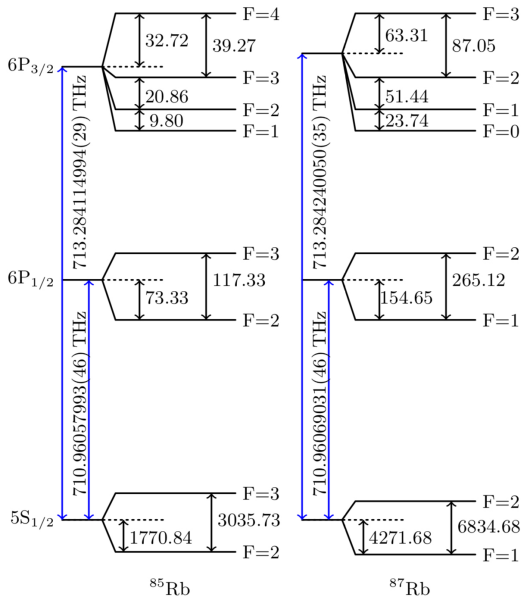

Figure 2.1: Rb^{85} and Rb^{87} energy level scheme for $5S_{1/2}$, $6P_{1/2}$ and $6P_{3/2}$ levels (not to scale) (taken from [10]). The hyperfine splitting is in units of MHz. The $6P_{1/2}$ state will not be regarded.

Isotope	$F_g \rightarrow F_e$	Freq. Offset [MHz]
Rb^{87}	$2 \rightarrow 1$	-1280.95
	$2 \rightarrow 2$	-1229.51
	$2 \rightarrow 3$	-1142.46
Rb^{85}	$3 \rightarrow 2$	-60.13
	$3 \rightarrow 3$	-39.27
	$3 \rightarrow 4$	0
	$2 \rightarrow 1$	2965.8
	$2 \rightarrow 2$	2975.6
	$2 \rightarrow 3$	2996.46
Rb^{87}	$1 \rightarrow 0$	5529.99
	$1 \rightarrow 1$	5553.73
	$1 \rightarrow 2$	5605.17

Figure 2.2: Possible transitions in Rb^{85} and Rb^{87} ($5S_{1/2} \rightarrow 6P_{3/2}$) considering hyperfine splitting of ground and excited state [10]. Frequency offset relative to Rb^{85} $5S_{1/2}(F = 3) \rightarrow 6P_{3/2}(F = 4)$.

2.2 High Temperature Spectroscopy Cell

A cylindrical glass cell with Rubidium vapor and a Rubidium reservoir is used to provide the Rubidium atoms for the spectroscopy (see figure 2.3(a)). The $5S_{1/2} \rightarrow 6P_{3/2}$ transition has a relatively low scattering cross section [13] and therefore a relatively low absorption coefficient, compared to the transition to the first excited state $5S_{1/2} \rightarrow 5P_{3/2}$ [14]. As a consequence the $5S_{1/2} \rightarrow 6P_{3/2}$ transition can not be observed properly at room temperature (unlike the $5S_{1/2} \rightarrow 5P_{3/2}$ transition). To increase the absorption coefficient the vapor pressure must be increased, which is achieved by heating the spectroscopy cell [15, 16]. In ref. [6] the spectroscopy was done at 150°C. The aim is to achieve a similar temperature.

Heating the vapor cell to high temperatures over a long period of time poses a challenge. At the coldest part of the cell the Rubidium vapor will cool down, condense and stick to the glass. To avoid losses in laser light transmission it is crucial to ensure that the cell windows are the hottest part of the vapor cell. This is realized by embedding a heating cartridge[3] into a copper block and mounting one of these blocks in front of each cell window (see figure 2.3(b)). For obvious reasons, the copper blocks require a hole for the laser beam to pass through. To minimize thermally induced stress in the glass cell, the copper blocks are not directly in contact with the cell windows. The temperature can be monitored via several temperature sensors, attached to different parts of the cell (and cell mount) (see figure 2.3(c)). The cell (including mount and copper blocks) is wrapped in multiple layers of aluminium foil to thermally insulate the whole contraption creating an oven for the cell (see figure 2.3(d)).

[3] *HT15W - 15 W Resistive Cartridge Heater* by Thorlabs. Nominal power of 15 W.

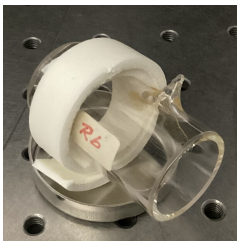

(a) Cylindrical Rubidium vapor cell made from glass and 5 cm long.

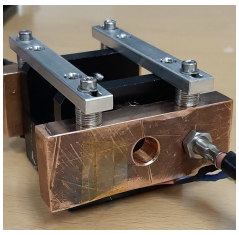

(b) Copper block in front of cell window.

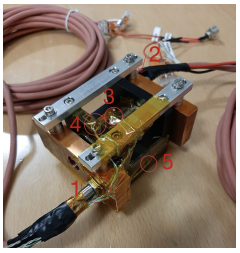

(c) Temperature sensors on the cell and its mount.

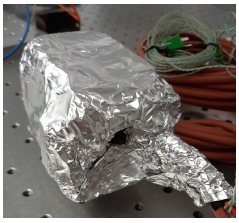

(d) Entire cell contraption insulated with aluminium foil

Figure 2.3: Pictures of the cell construction including temperature sensors for monitoring. Copper blocks to distribute heat and keep the windows from coating. Sensor 1,2 screwed into the copper blocks, Sensor 3 attached to the cell (halfway between each window), Sensor 4 attached to the mounting arm, Sensor 5 attached to the mounting block. Insulation to reach high temperatures (ideally >100°C).

2.2.1 Measurement and Results

To characterize the performance of the cell-heating setup, it is worth taking a look at the relation between input heating power and the resulting equilibrium temperatures at different points in the setup. This is depicted in figure 2.4.

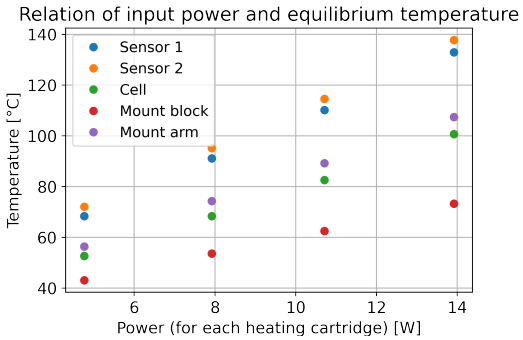

(a) Relation of input power (per cartridge) to equilibrium temperatures.

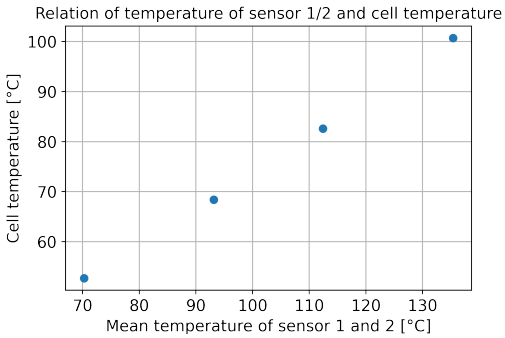

(b) Relation of the mean temperature of sensor 1 and 2 and temperature of the cell.

Figure 2.4: Plotting equilibrium temperatures against input power/mean temperature of the copper blocks to characterize the high temperature spectroscopy cell setup and its temperature distribution.

Since the equilibrium temperature is reached once the input power equals the effective loss rate, one would expect the relation between equilibrium temperature and input power to be described by the Stefan-Boltzmann law: $P = e\sigma A(T^4 - T_C^4)$ where P is the thermal energy radiation rate, e is the emissivity ($e = 1$ for an ideal black body), σ is Stefan's constant, A is the surface area of the object, T is its temperature and T_C is the surrounding temperature [17, 18]. This would lead to $T = \sqrt[4]{P/(e\sigma A) + T_C^4}$. The relations in figure 2.4(a) largely resembling a linear relation can be attributed to the fact, that the P-axis offset (due to the T_C^4 term) shifts the relation into a regime in which the graph approximately behaves linearly (over a relatively short temperature span). Also, the

cell contraption is far from being an idealised black body.

One can see that there is a slight discrepancy for sensor 1 and 2. This might be caused by the slight difference in size of the copper blocks, leading to different radiative losses. The fact that different sensors have different temperature slopes relative to the input power can be explained by a difference in heat conducted to each sensor (due to losses along the way).

With the heating cartridges in use, the cell can reach a temperature of about 100 °C. This can be improved by using more heating cartridges and using more aluminium foil to enhance the insulation. In the setup, 24 V can be applied to the heating cartridges. This yields a current of 0.58 A resulting in 13.92 W of power. The cartridges are rated to a nominal power of 15 W, which cannot be reached with the used power supply.

The relation between the temperature of the copper blocks and the cell temperature in figure 2.4(b) seems to resemble a linear relation, at least over the regime under consideration.

2.3 Absorption Spectroscopy (Doppler-broadened)

Absorption spectroscopy is a method to resolve energy levels of an atom. A laser drives the transition from ground state to excited state. The probability of excitation is dependent on the laser frequency with respect to the atomic transition frequency. The transmission of a laser through an atomic medium gives a so called *atomic spectrum*. This type of spectroscopy is also called Doppler-broadened spectroscopy, because the line shapes in the absorption spectrum are largely defined by Doppler-broadening.

2.3.1 Theory

The cause of Doppler-broadening is the thermal velocity distribution of the atoms (Maxwell-Boltzmann-distribution). At temperatures $T > 0\,\mathrm{K}$ atoms are not at rest but have a certain velocity $\vec{v}$. Thus they perceive the frequency of the laser light shifted by $\Delta\nu = \vec{k}\vec{v}$ with $\vec{k}$ being the wave vector. The intensity of the absorbed laser light can therefore be described the following way [19]:

$$I(\nu) \propto e^{\left(-4\ln(2)\left(\frac{(\nu-\nu_0)}{\Delta\nu_{\mathrm{FWHM}}}\right)^2\right)}. \tag{2.1}$$

Here, ν_0 is the transition frequency, and ν_{FWHM} is the width of the Doppler-broadened curve. This resembles a Gaussian distribution (see figure 2.8 (a)). The width can be calculated using [19]:

$$\Delta\nu_{\mathrm{FWHM}} = \frac{\nu_0}{c}\sqrt{\frac{8\log(2)k_B T}{m_{\mathrm{atom}}}}. \tag{2.2}$$

c is the speed of light, k_B the Boltzmann-constant, T the temperature in Kelvin and m_{atom} the mass of the atom. It becomes apparent that the ability to resolve certain energy level transitions is directly linked to the temperature of the atoms.

2.3.2 Setup

The basic setup for measuring Doppler-broadened transitions can be seen in figure 2.5. To be able to properly measure absorption spectra, one needs a laser whose frequency can be scanned thorugh the transition frequency. Here, a grating laser (*Toptica DL PRO 420*) is used. Since the laser frequency

scan also affects the output intensity of the laser, because the laser diode current is changed, one has to calibrate the signal of photodiode 1 by dividing it by the signal of the reference photodiode 2. Note that the half-wave plate (HWP) and polarizing beam splitter (PBS) are used to be able to adjust the ratio of light being focused onto photodiode 1 and 2. With this setup the $5S_{1/2}$ to $6P_{3/2}$ transitions of Rb^{85} and Rb^{87} can be measured.

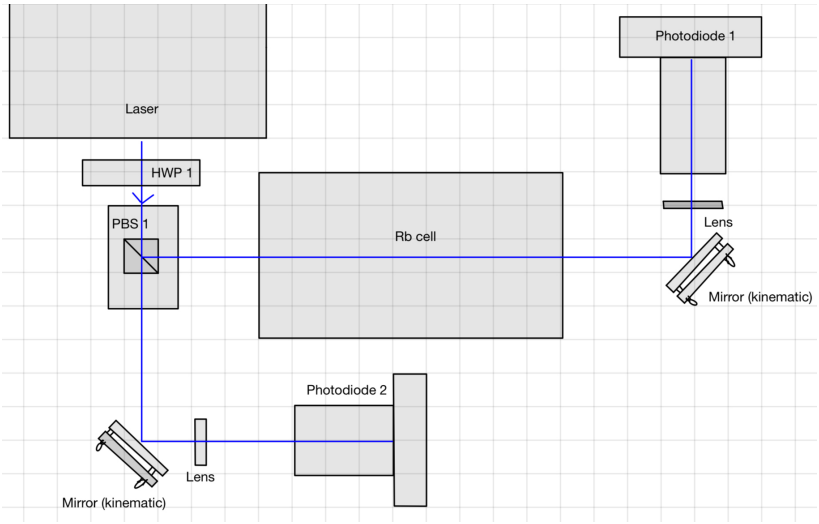

Figure 2.5: Basic setup to measure Doppler-broadened transitions. HWP used for adjusting intensity ratio of the split beams. Reference photodiode 2 to compensate changes in laser beam intensity caused by frequency scan.

2.3.3 Measurements and Results

Figure 2.5 illustrates the basic setup to measure Doppler broadened transitions. However, in chapter 3 the exact setup used for the spectroscopy measurements presented in this chapter is shown and discussed. For measuring the Doppler-broadened spectrum the pump beam was blocked.

Time Axis Calibration

The laser light intensity is measured as a function of time as the laser scans its frequency. Since there is no way to extract the information of the laser frequency directly at a given time, a calibration of the time axis is needed.

The measured spectrum in 2.6(a) has four distinct dips in photodiode voltage (i.e light intensity). It becomes apparent that the hyperfine splitting of the $6P_{3/2}$ state cannot be resolved. Only the $5S_{1/2}$ ($F = 2, 3$) to $6P_{3/2}$ (for Rb^{85}) and the $5S_{1/2}$ ($F = 1, 2$) to $6P_{3/2}$ (for Rb^{87}) transitions are visible (see table A.1). This is what is to be expected due to Doppler-broadening. Since the laser frequency (in this case) increases from left to right, one can identify the dips in signal amplitude as shown in figure 2.6(b).

Knowing the transition frequencies (see figure 2.1), the time axis can be calibrated by a fitting Gaussian curve to each observed transition using the fit function $f(x) = a \cdot e^{-\log(2)\cdot\left(\frac{x-c}{h}\right)^2} + mx + b$. The linear offset serves the purpose of cancelling out the residual overall signal slope. Such a slope

should have been removed by dividing with a reference signal, however, some slope remains. The difference between the positions of the Gaussian fits corresponds to a certain difference in frequency which is known. Thus the time axis can be calibrated. The fit(s) can be seen in figure 2.6(c) and 2.6(d). The corresponding fit parameters can be seen in table A.2 and A.3.

The difference in frequency of the Rb^{87} $5S_{1/2}$ $(F = 1)$ and $5S_{1/2}$ $(F = 2)$ to $6P_{3/2}$ is $\Delta\nu \approx 6.8347$ GHz (see figure 2.1 and table A.1). The difference in position of the respective dips in the absorption spectrum is (39.603 ± 0.019) ms. Therefore the calibration coefficient is $C_{\text{cal}} = (80.93 \pm 0.03)$ GHz/s.

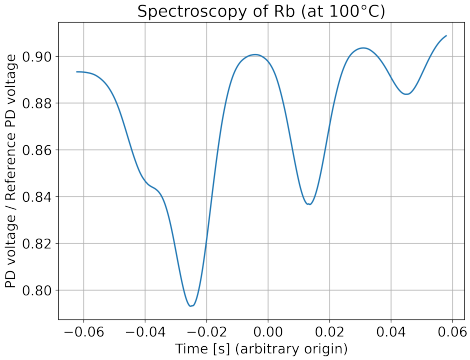

(a) Absorption spectrum of Rubidium at 100°C.

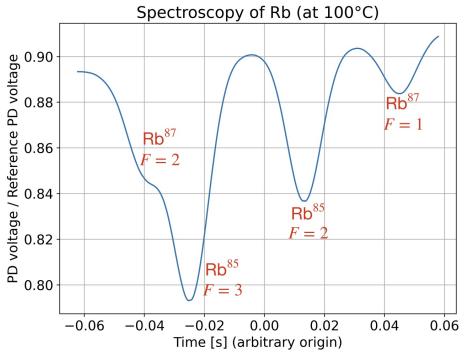

(b) Identification of the $5S_{1/2}$ to $6P_{3/2}$transitions observed in the absorption spectrum of Rubidium at 100°C.

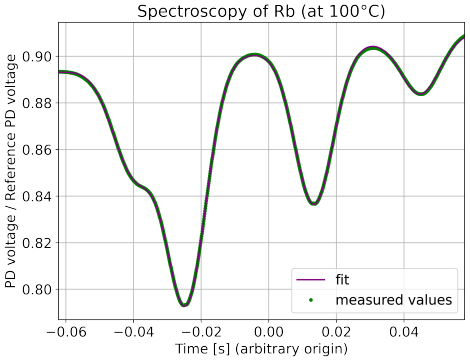

(c) Fitted absorption spectrum of Rubidium at 100°C. For fit parameters see table A.2

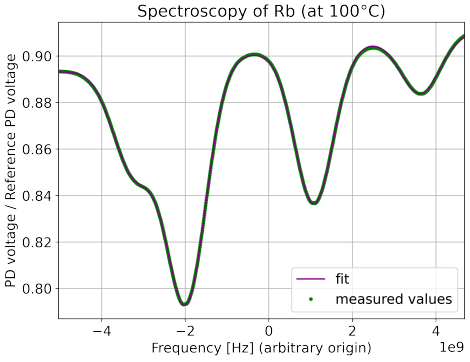

(d) Fitted absorption spectrum of Rubidium at 100°C with calibrated time/frequency axis. For fit parameters see table A.3.

Figure 2.6: Absorption spectrum of Rubidium at 100°C with identification of the observed transitions and a fit for the calibration of the time axis.

Comparing $\Delta\nu_{\text{FWHM}}$ to Theoretical Values

The Rb^{85} $5S_{1/2}$ $(F = 2)$ to $6P_{3/2}$ and the Rb^{87} $5S_{1/2}$ $(F = 1)$ to $6P_{3/2}$ transition are measured for different temperatures and subsequently fitted with the previously mentioned fit function. The fits are shown in figure A.1 and A.2. Their fit parameters can be found in tabel A.4 and A.5. The width of each transition $\Delta\nu_{\text{FWHM},i}$ can be calculated using the fit parameter h: $\Delta\nu_{\text{FWHM},i} = 2h_i \cdot C_{\text{cal}}$. These

widths can be found in table 2.1 and 2.2 with their corresponding theoretical value. A comparison of these widths and the theoretically expected widths (calculated using equation 2.2) is depicted in figure 2.7.

Temp. [°C]	$\nu_{\text{FWHM, exp}}$ [GHz]	$\nu_{\text{FWHM, theo}}$ [GHz]
53	(1.0139 ± 0.0023)	0.9980
67	(1.0071 ± 0.0013)	1.0192
78	(1.0182 ± 0.0009)	1.0355
91	(1.0511 ± 0.0005)	1.0545
100	(1.0786 ± 0.0031)	1.0675

Table 2.1: Widths of the Doppler-broadened transition of Rb^{85} ($F = 2$) to $6P_{3/2}$ and their corresponding theoretical values.

Temp. [°C]	$\nu_{\text{FWHM, exp}}$ [GHz]	$\nu_{\text{FWHM, theo}}$ [GHz]
53	(0.8790 ± 0.0005)	0.9897
67	(1.0192 ± 0.0031)	1.0107
78	(1.0550 ± 0.0031)	1.0269
91	(1.0262 ± 0.0012)	1.0457
100	(1.0608 ± 0.0012)	1.0586

Table 2.2: Widths of the Doppler-broadened transition of Rb^{87} ($F = 1$) to $6P_{3/2}$ and their corresponding theoretical values.

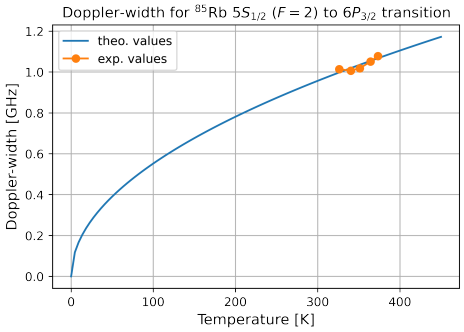

(a) Comparison of the theoretical widths of the Rb^{85} $5S_{1/2}$ ($F = 2$) to $6P_{3/2}$ transition due to Doppler-broadening and the measured widths.

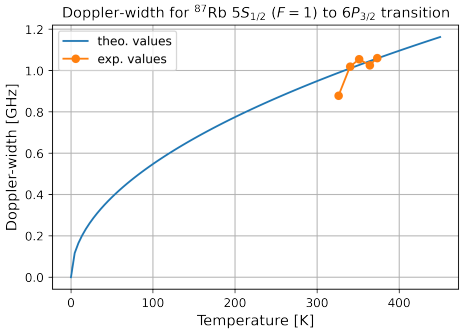

(b) Comparison of the theoretical widths of the Rb^{87} $5S_{1/2}$ ($F = 1$) to $6P_{3/2}$ transition due to Doppler-broadening and the measured widths.

Figure 2.7: Comparing theoretical widths due to Doppler-broadening with measured widths of different Rubidium transitions.

It becomes apparent that the measured widths largely resemble the theoretically expected trend. Even though the theoretical values are not in the area of error, they are very close. Deviations can have multiple causes. Firstly, there can always be a slight inhomogeneousness in temperature in the cell itself, leading to different temperatures contributing to the overall velocity distribution of the atoms and therefore resulting in possible inaccuracies of the fits. Secondly, especially for lower temperatures and smaller absorption, instability of the photodiode signal itself can cause a distortion of the measured absorption. This is likely what causes the width of the Rb^{87} $5S_{1/2}$ ($F = 1$) to $6P_{3/2}$ transition at 53 °C to deviate from the theoretical values as much as it does here. Thirdly, the natural linewidth is not considered. These widths should however be at least two orders of magnitude smaller than the $\Delta\nu_{\text{FWHM}}$ here[4]. Fourthly, other broadening effects like *pressure broadening* and *power broadening* are not accounted for here. For these reasons the measured $\Delta\nu_{\text{FWHM}}$ should tend to be larger than the theoretical width.

If all contributing broadening effects were known, one could use the measured widths to precisely calculate the temperature of the atoms.

[4] For example $\Delta\nu_{\text{nat}} = 1/(2\pi\tau) \approx 1.5\,\text{MHz} \ll 1\,\text{GHz}$ with $\tau = 109\,\text{ns}$ [20] for Rb^{87} $6P_{3/2}$.

2.4 Saturated Absorption Spectroscopy (Doppler-free)

The disadvantage of absorption spectroscopy is the fact that for one to be able to measure energy levels closely positioned to each other, one has to cool the atoms down drastically (depending on the atom and energy levels this might even get down to a few mK). Saturated absorption spectroscopy, a technique that it insensitive to Doppler-broadening, circumvents this issue.

2.4.1 Theory

For saturated absorption spectroscopy two counter-propagating overlapped laser beams are used. One beam, called the *pump beam*, drives the transition from ground state to excited state. For now a two-level system is assumed. Ideally the pump beam has an intensity so high that it approximately equalizes the population of ground state and excited state. The intensity of the other beam, the so called *probe beam*, is monitored on an oscilloscope. The beams usually share the same frequency, however, the intensity of the pump beam is much higher than probe beam intensity.

Here we assume the frequency of the beams to be not exactly equal to the transition frequency. Then there is a velocity component along the propagating axis of the beams $v_{\text{comp,z}}$ an atom needs to have to compensate the frequency detuning of the beams from the transition frequency (and get excited). But since the beams are counter-propagating, this velocity component $v_{\text{comp,z}}$ differs in sign. Thus the pump and probe beam interact with different classes of atoms as long as they are detuned from the resonance frequency. The intensity of the probe beam behaves like in absorption spectroscopy and is in this case not affected by the pump laser (see figure 2.8). However, when the frequency of the beams equals the transition frequency, the velocity component previously mentioned vanishes. Thus both beams interact with the same class of atoms[5]. Now the approximately equalized population in excited and ground state causes the probe beam to drive stimulated emission rather than excitation. As a consequence the effective absorption coefficient of the probe beam decreases (see figure 2.8) (hence the intensity monitored on the oscilloscope rises). The dips of the absorption coefficient are called *Lamb dips*.

The saturated-absorption coefficient can be described the following way [3]:

$$\alpha_s(\omega) = \alpha^0(\omega)\left[1 - \frac{S_0}{2}\frac{(\gamma_s/2)^2}{(\omega-\omega_0)^2 + (\Gamma_s^*/2)^2}\right]. \tag{2.3}$$

With $\alpha^0(\omega)$ being the Doppler-broadened part of the spectrum, $\Gamma_s^* = (\gamma + \gamma_s)/2$, $\gamma_s = \gamma\sqrt{1+S_0}$ with γ being the homogeneous linewidth and $S_0 = S_0(I, \omega_0)$ being the saturation parameter. This resembles a Lorentzian curve with a width close to the natural linewidth of the transition (for small S_0) [3, 19]. However, this equation is only adequate when dealing with low beam intensities relative to the saturation intensity $I_{\text{sat}} = 10.3\,\text{W/m}^2$ [21]. Is this not the case and other broadening effects are not negligible the form of the Lamb dips takes on a more complicated nature, a Voigt curve. This is a convolution of a Lorentzian and a Gaussian curve [19]. This, however, is not trivial to plot or fit.

In reality a lot of spectroscopy experiments deal with more complex energy level schemes than a simple two level system. For saturated absorption spectroscopy there is an additional phenomenon to consider called *cross-over resonance*. In figure 2.9 the underlying principle is illustrated. When the frequency of both pump and probe beam is exactly halfway between the resonance frequencies

[5] The ones with their velocity vector being perpendicular to the propagating axis of the beams.

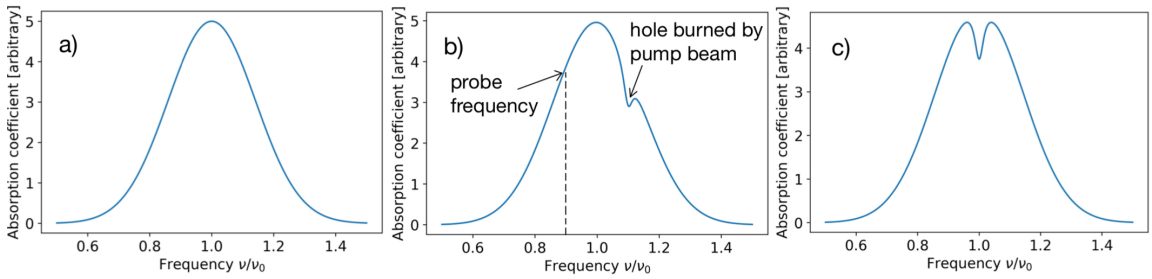

Figure 2.8: Visualization of the principle of saturated absorption spectroscopy for a two level structure with resonance frequency ν_0 and the origin of Lamb dips. Note that the ν-axis scale is just for visualization. In practise the Lamb dips are typically a lot closer to the actual resonance frequency than shown here.
a) displays the absorption coefficient of absorption spectroscopy. b) illustrates the case for off-resonant beams resulting in a dip in the absorption coefficient which, however, is not experienced by the probe beam. This is caused by counter propagation of the beams, which therefore interact with different classes of atoms. c) visualizes the case for resonant beams, causing the probe beam to experience the dip in the absorption coefficient caused by the pump beam (*Lamb dip*).

of two excited states ($|1\rangle$, $|2\rangle$), there are two classes of atoms which interact with the beams. The pump beam can excite one class to $|1\rangle$ and the other one to $|2\rangle$. For the probe beam it is the other way around. This leads to a third dip in absorption exactly inbetween the Lamb dips corresponding to the transitions to $|1\rangle$ and $|2\rangle$. This is illustrated in figure 2.10.

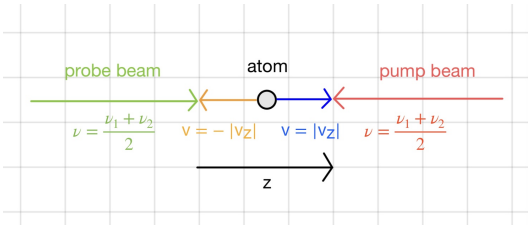

(a) Visualization of Doppler-shift of an atom relative to pump and probe beams.

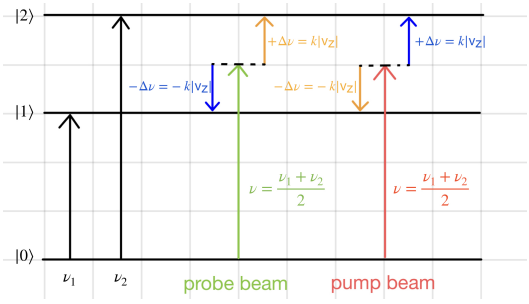

(b) Visualization of Doppler-shift in energy level scheme causing crossover dips.

Figure 2.9: Visualizations of the cause of crossover dips.

2.4.2 Setup

As mentioned before, saturated absorption spectroscopy mainly differs from absorption spectroscopy by utilizing two laser beams instead of one. The setup has to be adjusted accordingly and can be seen in figure 2.11.

With HWP 1 one can adjust the ratio of light going to the reference photodiode and to the rest of the setup. HWP 2 determines the proportions of intensity of pump and probe beam. HWP 3 is used to control the intensity of the pump beam independently. It is absolutely crucial that the pump and probe beam are superimposed!

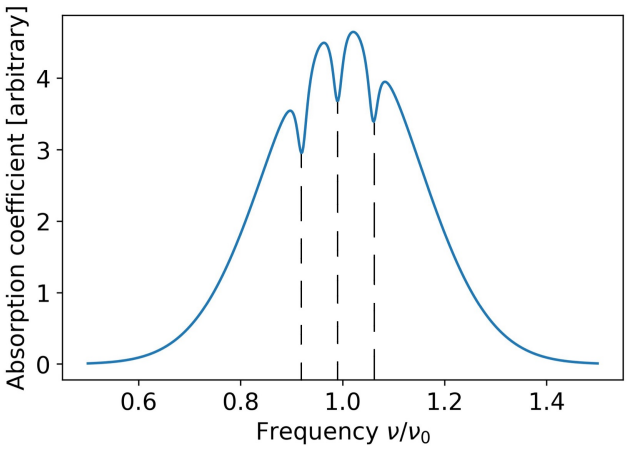

Figure 2.10: Visualization of the position of the crossover resonance relative to the Lamb dips of the actual transitions. It is important to remark that the crossover resonance peak is exactly halfway between the two Lamb dips. Note that the ν-axis scale is just for visualization. In practise the Lamb dips are typically a lot closer to the actual resonance frequency than shown here.

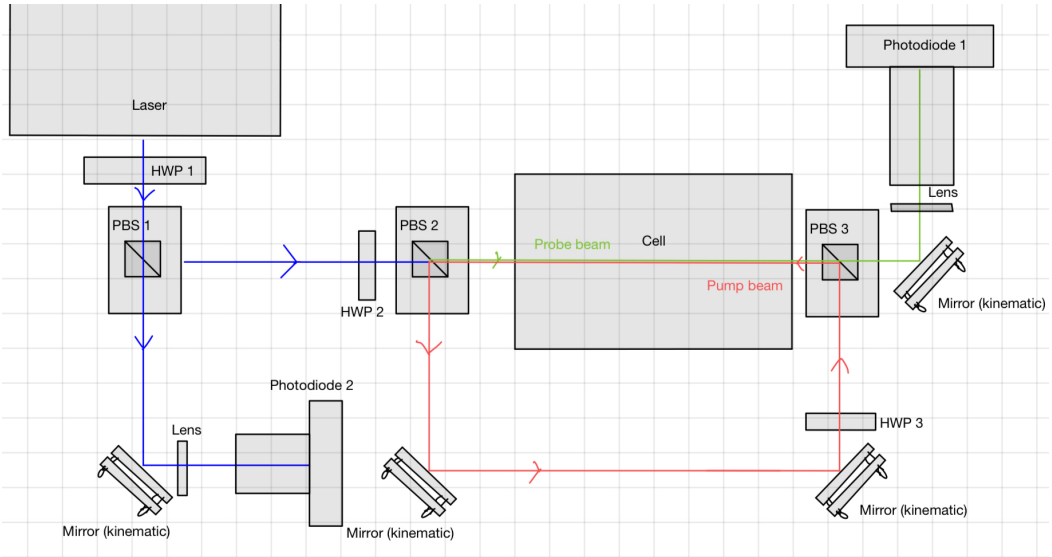

Figure 2.11: Basic setup for saturated absorption spectroscopy. Photodiode 2 used as a reference to compensate the change in laser intensity throughout the frequency scan. Waveplates used in combination with PBS to adjust the intensity ratio of the split beams. Superimposition of pump and probe beam is achieved by adjusting the position/orientation of the corresponding mirrors.

2.4.3 Measurements and Results

Figure 2.11 shows the necessary setup for saturated absorption spectroscopy. The exact setup used for the measurements in this section (see figure 3.1) is discussed in chapter 3.

The entire Doppler-free spectrum can be seen in figure 2.12. The Doppler-free spectrum clearly shows the general Doppler-broadened line shape of the different transitions with the Lamb dips peaking through at each transition due to the method of saturated absorption spectroscopy.

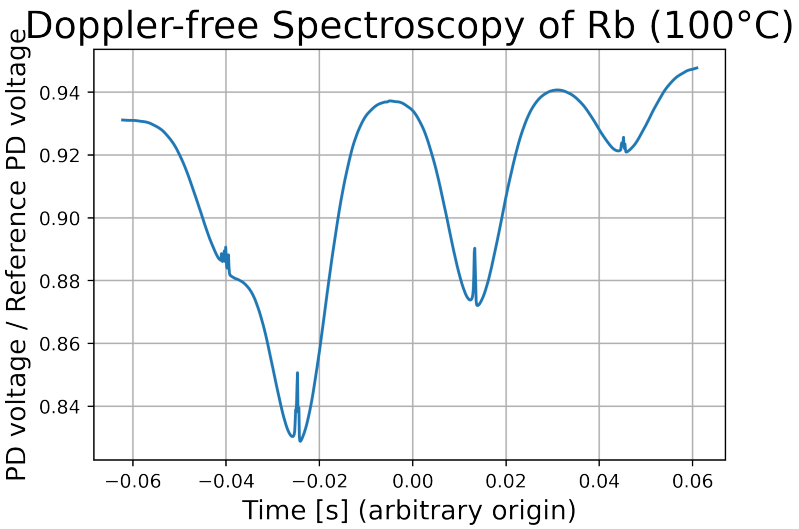

Figure 2.12: Doppler-free absorption spectrum of Rubidium at 100°C. The Doppler-broadened shape of the transitions (with hyperfine splitting of the ground state) is visible. The lamb dips correspond to hyperfine structure of the excited state which can be resolved with saturated absorption spectroscopy.

Identification and Characterisation of Lamb Dips

The measured Lamb dips are depicted in figure 2.13(a), 2.13(d), 2.13(g) and 2.13(i) and can be identified as seen in figure 2.13(b), 2.13(e), 2.13(h) and 2.13(j). It has to be mentioned, that the Lamb dips of the Rb^{85} $5S_{1/2}$ $(F = 2)$ to $6P_{3/2}$ are not properly resolved and therefore can not be easily identified. However, the position of four Lamb dips/crossover resonances can be roughly estimated (see red lines in figure 2.13(h)). Still, further analysis of these dips does not seem reasonable. Despite this, the Lamb dips and crossover resonances of the other transitions seem to adhere to what is theoretically expected. For each transition there are three Lamb dips with crossover resonances halfway between the corresponding Lamb dips.

To precisely analyze the differences in frequency of the Lamb dips and crossover resonances, one can fit a Lorentzian curve to each:

$$f_i(\nu) = \frac{a_i}{(\nu^2 - c_i^2)^2 + h_i^2 c_i^2}. \tag{2.4}$$

The fit function is a superposition of six Lorentzian curves with a linear offset:

$$f(\nu) = \left(\sum_{i=1}^{6} f_i(\nu) \right) + m\nu + b. \tag{2.5}$$

The linear offset is employed to compensate the fact, that the lamb dips are not completely centered in the Doppler-broadened dips. The fits can be seen in figure 2.13(c), 2.13(f) and 2.13(k). The corresponding fit parameters can be found in table A.6, A.8 and A.10. From the fit parameters, the resonance amplitude A and $\Delta\nu_{\mathrm{FWHM}}$ can be determined:

$$A = \frac{a}{h^2 c^2} \tag{2.6}$$

$$\Delta\nu_{\mathrm{FWHM}} = \sqrt{c^2 + hc} - \sqrt{c^2 - hc}. \tag{2.7}$$

These parameters can be found in table A.7, A.9 and A.11. The comparison of experimental and theoretical values of the frequency difference between two Lamb dips and their corresponding cross-over resonance is shown in table 2.3, 2.4 and 2.5. The theoretical values can be calculated using figure 2.1 and table 2.2. Looking at these values, it becomes apparent, that the experimental values largely validate each other: even though their error bars hardly overlap, most Lamb dips share a very similar frequency difference to their corresponding cross-over resonance. Regarding the comparison to the theoretical values, it can be said, that the theoretical values tend to be slightly larger than the experimental ones. Considering the experimental values are relatively consistent with each other, this leads to believe that the measurement is sufficiently precise but its accuracy is impaired due to a systematic erro. This error is likely an inaccuracy in the calibration performed in 2.3.3. It has to be mentioned, that with table 2.5 it becomes apparent that the identification of the Rb^{87} $5S_{1/2}$ $(F = 1)$ to $6P_{3/2}$ $(F = 0)$ transition is not correct. The experimental value is almost twice the other corresponding experimental value. The same is true for the according theoretical value. In the spectrum, however, there is no other dip that could correspond to this transition. It is possible, that the laser has a mode hop close to this transition. But, even when recording this spectrum several times with different laser settings there is no peak visible that is closer to the corresponding cross-over resonance. It is possible that the actual peak has such a low amplitude, that it is hidden in the crossover resonance. In that case, the falsely identified peak might just be noise. The frequency where the Lamb dip is expected to be can is shown in figure 2.13(j).

F_1 and F_2	Exp./Theo.	$\Delta\nu(F_1 \leftrightarrow \mathrm{Co}(F_1/F_2))$ [MHz]	$\Delta\nu(\mathrm{Co}(F_1/F_2)) \leftrightarrow F_2)$ [MHz]
1 and 2	Exp.	(24.73 ± 0.17)	(24.75 ± 0.06)
	Theo.	25.72	25.72
1 and 3	Exp.	(67.00 ± 0.16)	(67.29 ± 0.03)
	Theo.	69.25	69.25
2 and 3	Exp.	(42.47 ± 0.05)	(42.34 ± 0.03)
	Theo.	43.53	43.53

Table 2.3: Comparing the frequency differences between lamb dips and their cross-over resonances for experimental and theoretical values for the Rb^{87} $5S_{1/2}$ $(F = 2)$ to $6P_{3/2}$ transitions. Theoretical values taken from [10].

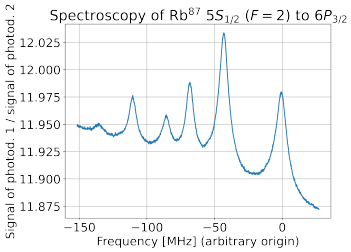

(a) Lamb dips for the Rb^{87} $5S_{1/2}$ $(F = 2)$ to $6P_{3/2}$ $(F = 1, 2, 3)$ transitions.

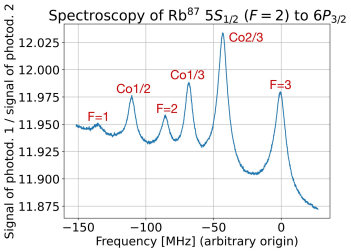

(b) Identified Lamb dips for the Rb^{87} $5S_{1/2}$ $(F = 2)$ to $6P_{3/2}$ $(F = 1, 2, 3)$ transitions.

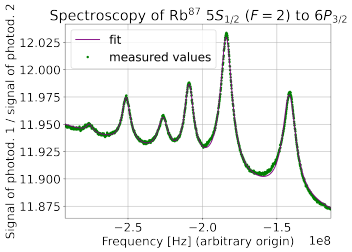

(c) Fitted Lamb dips and cross-over resonances for Rb^{87} $5S_{1/2}$ $(F = 2)$ to $6P_{3/2}$ $(F = 1, 2, 3)$ transitions.

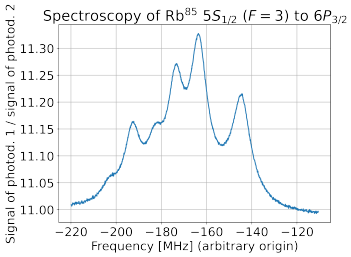

(d) Lamb dips for the Rb^{85} $5S_{1/2}$ $(F = 3)$ to $6P_{3/2}$ $(F = 2, 3, 4)$ transitions.

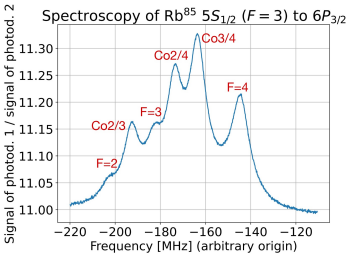

(e) Identified Lamb dips for the Rb^{85} $5S_{1/2}$ $(F = 3)$ to $6P_{3/2}$ $(F = 2, 3, 4)$ transitions.

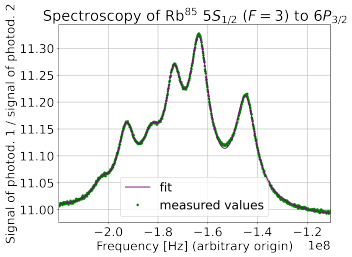

(f) Fitted Lamb dips and cross-over resonances for Rb^{85} $5S_{1/2}$ $(F = 3)$ to $6P_{3/2}$ $(F = 2, 3, 4)$ transitions.

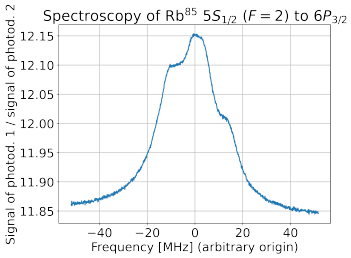

(g) Lamb dips for the Rb^{85} $5S_{1/2}$ $(F = 2)$ to $6P_{3/2}$ $(F = 1, 2, 3)$ transitions.

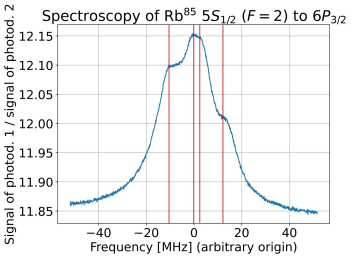

(h) Not fully identified Lamb dips for the Rb^{85} $5S_{1/2}$ $(F = 2)$ to $6P_{3/2}$ $(F = 1, 2, 3)$ transitions.

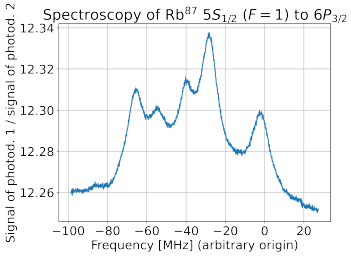

(i) Lamb dips for the Rb^{87} $5S_{1/2}$ $(F = 1)$ to $6P_{3/2}$ $(F = 0, 1, 2)$ transitions.

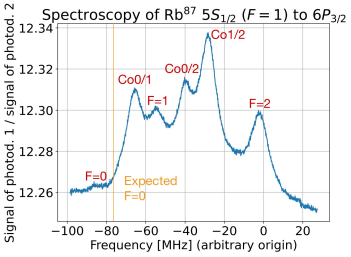

(j) Identified Lamb dips for the Rb^{87} $5S_{1/2}$ $(F = 1)$ to $6P_{3/2}$ $(F = 0, 1, 2)$ transitions.

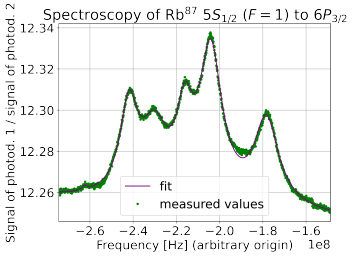

(k) Fitted Lamb dips and cross-over resonances for Rb^{87} $5S_{1/2}$ $(F = 1)$ to $6P_{3/2}$ $(F = 0, 1, 2)$ transitions.

Figure 2.13: Lamb dips for the Rb^{85} $5S_{1/2}$ to $6P_{3/2}$ transitions including identification and fit.

F_1 and F_2	Exp./Theo.	$\Delta\nu(F_1 \leftrightarrow \mathrm{Co}(F_1/F_2))$ [MHz]	$\Delta\nu(\mathrm{Co}(F_1/F_2 \leftrightarrow F_2))$ [MHz]
2 and 3	Exp.	(10.06 ± 0.09)	(10.17 ± 0.05)
	Theo.	10.43	10.43
2 and 4	Exp.	(29.20 ± 0.08)	(28.81 ± 0.02)
	Theo.	30.70	30.70
3 and 4	Exp.	(19.15 ± 0.04)	(18.62 ± 0.02)
	Theo.	19.64	19.64

Table 2.4: Comparing the frequency differences between lamb dips and their cross-over resonances for experimental and theoretical values for the Rb^{85} $5S_{1/2}$ $(F = 3)$ to $6P_{3/2}$ transitions. Theoretical values taken from [10].

F_1 and F_2	Exp./Theo.	$\Delta\nu(F_1 \leftrightarrow \mathrm{Co}(F_1/F_2))$ [MHz]	$\Delta\nu(\mathrm{Co}(F_1/F_2) \leftrightarrow F_2))$ [MHz]
0 and 1	Exp.	(20.42 ± 0.27)	(11.80 ± 0.09)
	Theo.	11.87	11.87
0 and 2	Exp.	(46.23 ± 0.26)	(37.83 ± 0.05)
	Theo.	37.59	37.59
1 and 2	Exp.	(26.08 ± 0.08)	(25.75 ± 0.04)
	Theo.	25.72	25.72

Table 2.5: Comparing the frequency differences between Lamb dips and their cross-over resonances for experimental and theoretical values for the Rb^{87} $5S_{1/2}$ $(F = 1)$ to $6P_{3/2}$ transitions. Theoretical values taken from [10].

Dependence of Lamb Dip Amplitude on Pump and Probe Beam Power

Figure 2.14 shows the Lamb dips and cross-over resonances for the $5S_{1/2}$ $(F = 3)$ to $6P_{3/2}$ $(F = 2, 3, 4)$ transitions for different pump beam powers. It becomes apparent, that the peak amplitude increases with rising pump power. However, their width also increases considerably. To find an optimal power (ratio) it is important to analyze these dips more quantitatively. For higher powers, a simple Lorentzian fit is not adequate. In that case they resemble a Voigt curve [3]. As mentioned before in section 2.4.1 it is not trivial to fit this sort of curve. Due to time restraints, no suitable fits are achieved.

The fact that the lamb dips are not perfectly centered in the Doppler-broadened dip might serve as an explanation as to why the photodiode signal is not the same on each side of the spectrum in figure 2.14.

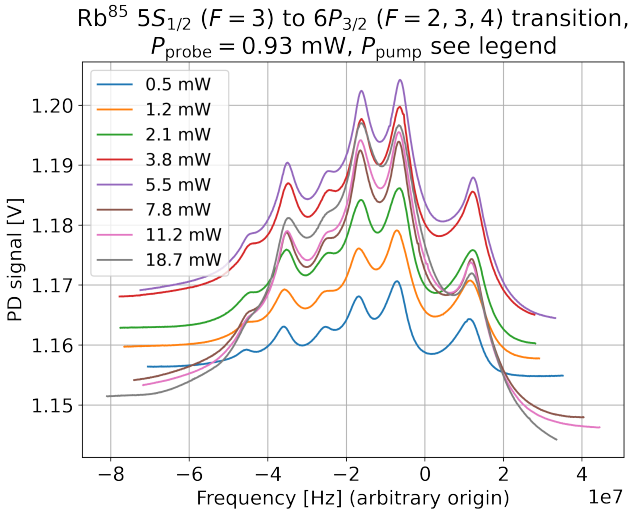

Figure 2.14: Lamb dips and cross-over resonances for the $5S_{1/2}$ ($F = 3$) to $6P_{3/2}$ ($F = 2, 3, 4$) transitions for different pump beam powers. Note that the drift of the laser frequency between measurements was manually compensated by adding a frequency shift to the data for better visible comparison.

CHAPTER 3

Modulation Transfer Spectroscopy (MTS)

In the previous chapter, the saturated absorption spectrum of the $5S_{1/2} \rightarrow 6P_{3/2}$ transition in for Rb^{85} and Rb^{87} was shown. The overall goal is to use this signal to frequency-stabilize the laser. Here, this is done with modulation transfer spectroscopy (MTS). The idea of MTS is that frequency sidebands are modulated onto the pump beam using an electro-optical modulator (EOM). The nonlinear[1] optical medium, in this case the atomic vapor, transfers the sidebands onto the probe beam. With the relative phase between the probe beam and its frequency sidebands an error signal for frequency-stabilization can be created. Therefore, apart from the high temperature spectroscopy cell the key element for MTS is an electro-optical modulator (EOM) to create frequency sidebands.

In this chapter section 3.1 discusses the theoretical background of EOMs and modulation transfer spectroscopy. In section 3.2 the experimental setup is explained. Section 3.3 deals with the characteristics of the EOM, the phase modulation achieved by it as well as the creation of frequency sidebands and the creation of the error signals for MTS.

3.1 Theory

3.1.1 Electro-optical Modulator (EOM)

Electro-optical modulators are devices used to modulate light in frequency, phase, amplitude or polarisation. In most cases EOMs are birefringent crystals. Here a lithium niobate ($LiNbO_3$) crystal is used. Their refractive indices n_o (ordinary) and n_e (extraordinary) can be influenced by an externally applied electric field, typically realised by inserting the crystal in between capacitor plates. This effect is called the *Pockels effect* [22]. The *Pockels coefficients* characterize the change of the refractive index depending on the orientation of the crystal and the polarisation of light. However, here, only a linearly polarized beam horizontal to the face of the EOM crystal is considered (see section 3.2.1). Thus only one pockels coefficient (r_{33}) contributes to the change of the refractive index (for more information see ref. [23]). The change of the (extraordinary) refractive index can then be described by the following equation [23]:

$$\frac{1}{n_e'(E)} = \frac{1}{n_e(0)} + r_{33}E. \tag{3.1}$$

[1] the nonlinearity is achieved by saturation of the optical medium.

With $n_e(E)$ being the altered extraordinary refractive index, E being the applied E-field and $n_e(0)$ being the unaltered extraordinary refractive index. For $r_{33}E \ll n_o^{-2}$ this equation can be approximated to be [23]:

$$n_e(E) \approx n_e(0) + \frac{1}{2}n_e^3 r_{33} E \tag{3.2}$$

$$n_e(E) - n_e(0) \approx \frac{1}{2}n_e^3 r_{33} E. \tag{3.3}$$

This change of the refractive index leads to a phase shift which can be calculated using the following equation [23]:

$$\Delta\phi(E) = \phi(E) - \phi(0) = k_0[n_e(E) - n_e(0)]L = \frac{\pi n_e^3 r_{33} L}{\lambda_0} E \tag{3.4}$$

with k being the wave vector, L being the length of the crystal (in the direction of propagation of the light). SincetThe E-field is typically applied by placing capacitor plates on either side of it, effectively forming a capacitor, one can now use $E = V/d$ with V being the applied voltage and d the distance between the capacitor plates to get:

$$\Delta\phi(V) = \frac{\pi n_e^3 r_{33} L}{\lambda_0 d} V. \tag{3.5}$$

As a result one can define the voltage V_π needed to achieve a phase shift of π:

$$V_\pi = \frac{\lambda d}{n_e^3 r_{33} L}. \tag{3.6}$$

The voltage V_π is typically in the order of magnitude of several 100 V. If the EOM is driven by a sinusoidal signal with modulation index M and frequency ω_m [2], the pump light wave can be written as [24]:

$$E_{\text{pump}}(t) = E_0 \cos(\omega t + M \sin(\omega_m t)). \tag{3.7}$$

Using Fourier decomposition one can write $E_{\text{pump}}(t)$ as [24]:

$$E_{\text{pump}}(t) = E_0 \sum_{k\in\mathbb{Z}} J_k(M) \cos((\omega + k\omega_m)t) \tag{3.8}$$

with $J_k(M)$ being Bessel functions of the first kind. This shows the splitting of the pump beam into a carrier frequency ω with frequency sidebands $\omega \pm k\omega_m$. It has to be noted that the amplitude of sidebands typically falls off drastically with higher values of k.

3.1.2 Modulation Transfer and Error Signal Creation

The probe beam, pump beam and its sidebands create a fourth wave with frequency $\omega \pm k\omega_m$ (because of the conservation of energy) propagating in the direction of the probe beam (because of the

[2] In practise, this sort of driving signal is often realized with a resonance circuit.

conservation of momentum) through degenerate four-wave mixing (DFWM) [24, 25]. This constitutes a complete transfer of modulation from the pump to the probe beam [24]. For more detail see ref. [25].

The error signal used to frequency-stabilize the laser to is generated by demodulating the probe beam signal with a signal identical to the EOM driving signal with adjustable amplitude M and phase ϕ. As discussed in ref. [24], the resulting function is odd with respect to the frequency detuning and 0 at resonance. These are desirable characteristics for a signal used for frequency-stabilization of a laser.

The optimization of the quality of the error signal is also discussed in [24]. It is argued, that finding suitable combinations of M, ω_m and ϕ is not straight forward, since the phase ϕ_a for maximizing the amplitude of the error signal is not identical to the phase ϕ_s for maximizing the slope of the error signal at resonance. Additionally, $\phi_{a,s}$ depends on M and ω_m. Usually the modulation frequency is chosen such that $\omega_m \ll \gamma$ with γ being the width of the structure in the optical spectrum one wants to use as a stabilization reference. For more detail see ref. [24].

3.2 Setup

Figure 3.1 shows the optical setup used in this thesis to do modulation transfer spectroscopy. The output beam from the laser is coupled into a polarization-maintaining fiber to achieve a clean mode while avoiding polarization drifts caused by the fiber. The PBS 0, waveplates HWP 0,1 and QWP 0 are used to adjust the polarization and to compensate potential inaccuracies of the polarization-maintaining fiber. The beam is then coupled out and split into one beam, which is focused on the reference photodiode and another one which is subsequently split again. One part of the beam is coupled into a fiber leading to a wavemeter, the other part is split yet again into a pump and probe beam. The probe beam passes through the cell and is then focused onto a photodiode. The signal of the photodiode is passed through a DC-block, then through a low-pass and two amplifiers to the R-port of a mixer, as shown in figure 3.2. The pump beam is phase-modulated by the EOM, driven by a signal generator to create frequency sidebands. For this, it has to be made sure that the laser beam is linearly polarized horizontally relative to the face of the EOM crystal (and therefore the optical axis of the crystal)since the electric field is applied along this axis. An identical signal to the EOM driving signal (with a tunable phase shift) is put into the L-port of the mixer. The modulation transferred from the pump to the probe beam is then mixed down by the mixer to create a beat note at each Lamb dip the laser is scanning through. This signal constitutes the error signal which can be used to frequency-stabilize the laser.

3.2.1 EOM

The EOM used in this thesis is shown in figure 3.3(a). The EOM crystal is placed between a conductive metal plate and a copper strip, effectively forming a capacitor (see 3.3(b)). The metal plate simultaneously forms the back wall of the whole EOM contraption. It is connected with the ground of the SMA-port mounted to it. The copper strip is connected to a coil ($L = 220\,\mu$H) which is connected to the other pole of the SMA-port. This constitutes a resonance circuit. For impedance-matching, a capacitor ($C_M = 68$ pF) is put in series to the resonance circuit 3.3(c).

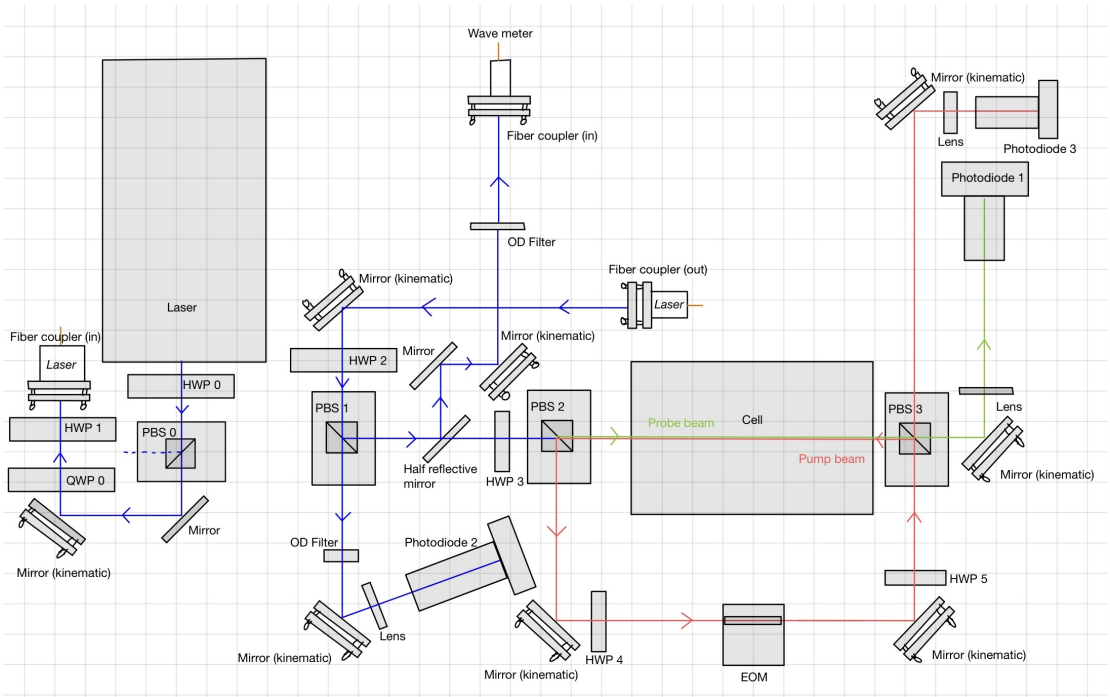

Figure 3.1: Optical setup for frequency-stabilizing a laser to Rubidium transitions using MTS. Waveplates in combination with PBS used for adjusting the intensity ratio of the split beams respectively. The EOM modulates frequency sidebands on the pump beam. This modulation is then transferred to the pump beam. The signal of photodiode 1 can be used as shown in figure 3.2 to create the error signal for frequency-stabilisation.

3.2.2 Pockels Cell for Measuring Phase Modulation

For measuring the amount of modulation achieved with the EOM the setup shown in figure 3.1 has to be adjusted. The most straight forward method for measuring this is to use a Pockels cell (see ref. [26] for more detail), since the pure phase modulation achieved by the EOM setup[3] can not be easily measured itself. Turning HWP 4 until the plane of polarization is at a 45° relative to the (extra-)ordinary axis of the crystal causes equal parts of the beam to experience the ordinary and extraordinary refractive index respectively. This leads to a phase shift between the different parts of the beam, effectively changing the polarization from diagonal relative to the optical axis of the crystal to elliptical, then circular (at 90° phase shift) then elliptical again to ultimately anti-diagonal (at 180° phase shift). HWP 5 has to be adjusted in such a way that it functions as a linear polarizer (together with PBS 3) turned 90° relative to the polarization of the incident beam in front of the EOM. This way, one can measure the amount by which the EOM turns the plane of polarization as a function of the applied voltage by measuring the pump beam light intensity transmitted by PBS 3 and focused onto photodiode 3.

[3] As a reminder: Only the phase is modulated since the laser beam is linearly polarized horizontally to the face of the crystal, along the extraordinary axis.

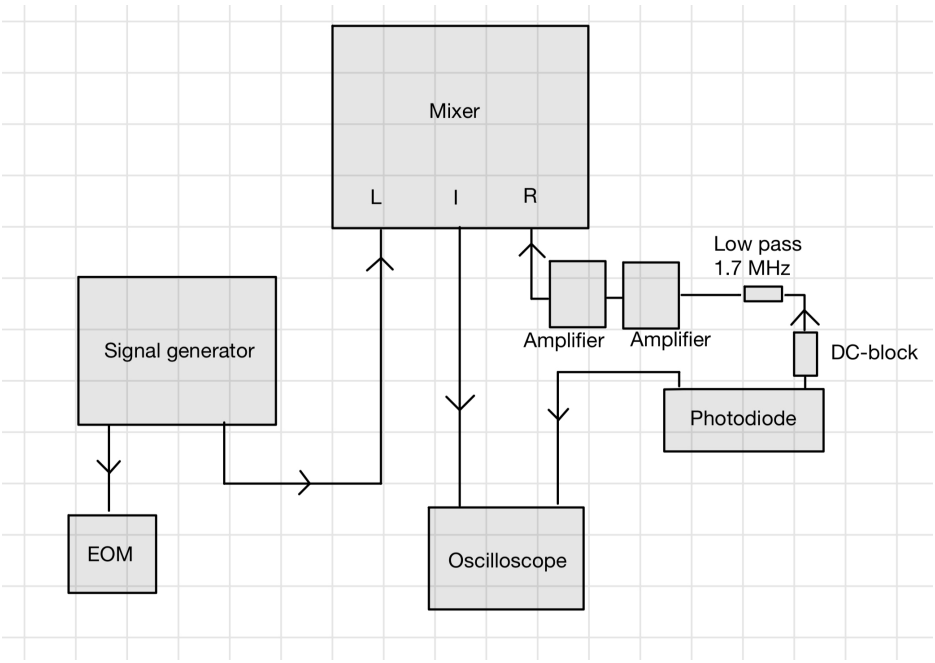

Figure 3.2: Wiring for demodulation of the probe beam signal and creation of error signals to use for frequency-stabilization. DC-block eliminates the DC-component, only the AC-component of the signal is necessary. Low-pass employed to reduce low-frequency noise (while actual signal is unaffected). Amplifiers are used to increase the error signal amplitude. The EOM is driven with a signal generator. The same signal, with an adjustable phase difference, is used for the demodulation of the probe beam signal.

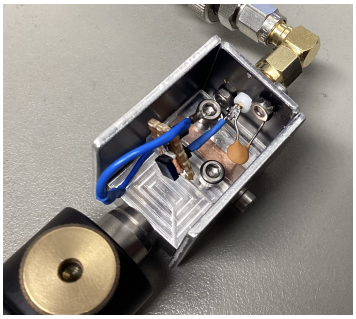

(a) Contraption to employ a (free space) EOM crystal including resonance circuit in an optical setup.

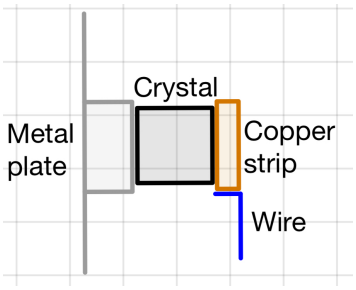

(b) Sketch of a frontal view on the EOM contraption.

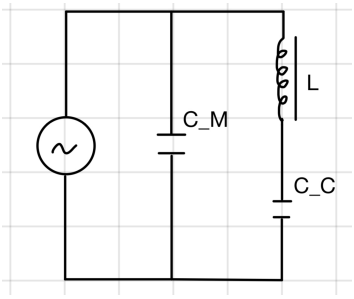

(c) Sketch of the EOM circuit with C_C being the EOM crystal capacity, L being the inductivity and C_M being the capacity for impedance-matching.

Figure 3.3: Explanatory pictures to illustrate the functionality of the EOM setup.

3.3 Measurements and Results

3.3.1 Characterization of the EOM (circuit)

EOM Circuit Resonance

To characterize the EOM resonance circuit, a network analyzer is used to measure the EOM resonance frequency. The measured resonance of the EOM circuit is depicted in figure 3.4 (see figure 3.4(a) for the amplitude and figure 3.4(b) for the phase). The seemingly discrete steps in amplitude/phase are caused by the minimal resolution of the network analyzer that is used to measure the resonance at hand. It is also important to mention, that the phase jump at the resonance frequency is not equal to the typical phase jump of a resonance of 180°. This can be attributed to the relatively low resonance amplitude. It is expected that the phase jump approaches 180° for a sufficiently high resonance amplitude.

To accurately determine the resonance frequency of the EOM circuit, the resonance is fitted with a Lorentzian curve (see equation (2.4)). The fit can be seen in figure 3.4(c). The fit parameters can be found in table A.12. The resonance frequency is (3.533 ± 0.001) MHz. It has to be noted here that disturbances in the resonance cause the fit to have slight inaccuracies regarding the resonance frequency. These disturbances are discussed later. The amplitude $A = (-3.86 \pm 0.11)$ dBm equals (41.1 ± 0.1) % of the power being reflected back. One wants as much power to remain in the resonance circuit as possible since the phase modulation scales linearly with the applied voltage. This is typically achieved by adjusting C_M to optimize the impedance-matching.

Impedance-matching of the EOM Resonance Circuit

In figure 3.4(d) resonances for different C_M are depicted. It becomes apparent that the amplitudes of the resonances does not surpass the $A = (-3.86 \pm 0.11)$ dBm significantly. The fact that the impedance of the coil, used in the resonance circuit, might have a real part (apart from the imaginary part), which exceeds the impedance against which the circuit is supposed to be matched, might serve as an explanation as to why this is the case. Placing an additional inductor in series with the entire resonance circuit should suffice to solve this issue. Still, the amplitude achieved here is deemed sufficient for now.

Another observation to be made is the fact that the resonance frequencies in figure 3.4(d) are not all equal. This may be caused by slight changes in the position and orientation of wires in the resonance circuit while handling the EOM contraption. To minimize this issue it is advisable to manufacture a suitable housing for the EOM contraption.

Disturbances in the EOM Resonance

One can also observe disturbances in the amplitude as well as in the phase of the resonance. The fact that the EOM crystal ($LiNbO_3$) has both electro-optic and piezo-electric properties [27] might serve as an explanation for these disturbances. Because of the piezo-electric effect the signal driving the EOM does not only modulate the refractive index (and therefore the phase of the light passing through it) but also the thickness of the crystal itself. This influences the capacity of the crystal thus altering the resonance frequency of the circuit resulting in a change in the signal amplitude. Therefore, the disturbances in amplitude and phase of the resonance might be different orders of several mechanical

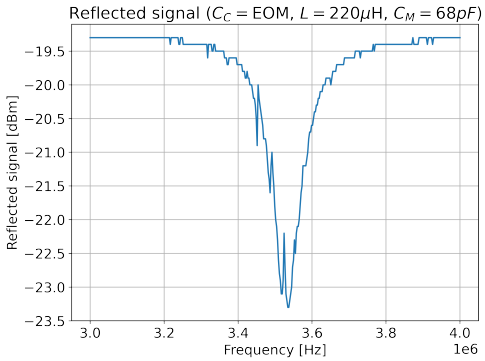

(a) Reflected signal amplitude of the EOM circuit.

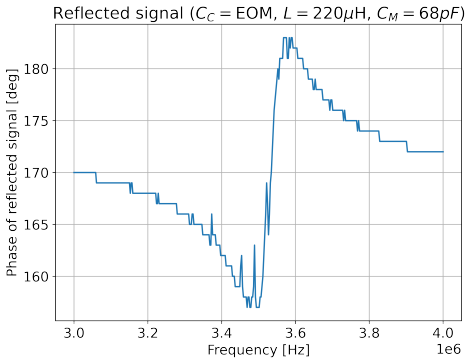

(b) Reflected signal phase of the EOM circuit.

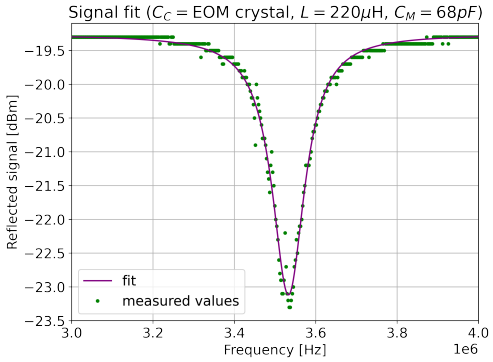

(c) Lorentzian curve fitted to the EOM circuit resonance. For fit parameters see table A.12.

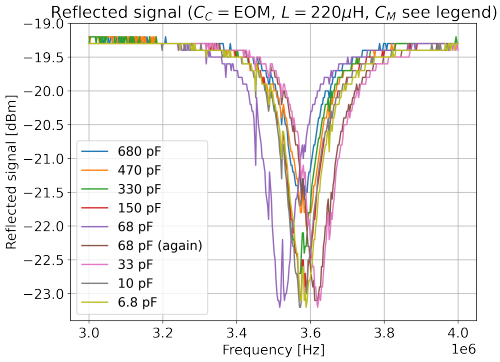

(d) Measured resonances of the EOM circuit for different impedance-matching capacities C_M.

Figure 3.4: Measured EOM circuit resonances including resonance amplitude fit and resonance amplitudes for impedance matching.

oscillation modes of the EOM crystal. The disturbances caused by different orders of a single mode appear periodically (with $\Delta\nu_{\mathrm{FSR}}$) whereas multiple types of modes might have different $\Delta\nu_{\mathrm{FSR}}$ to begin with. The fact that these disturbances are caused by mechanical oscillations also explains why these disturbances only appear in close proximity to the resonance frequency, i.e. when there is a considerable voltage applied to the crystal capacitor. Effects like impedance-mismatching due to imperfections in cables or BNC-connectors would be visible throughout the whole frequency scan.

3.3.2 Laser Light Modulation

Estimation of the Amount of Modulation

Using the adjusted setup to effectively employ a Pockels cell as described in section 3.2.2 one can record the light intensity transmitted by the Pockels cell relative to the modulation voltage applied to the EOM. Here a sinus signal with the resonance frequency of the EOM is used as the EOM driving signal. The resulting graphs can be seen in figure 3.5(a). With the sinus signal applied to the EOM, the phase shift between the two components of the beam (one polarized parallel and one

perpendicular to the optical axis of the crystal) is modulated. This changes the intensity of transmitted light periodically, adhering to Malus' law. However, this phase shift is not scanned linearly with time since the modulation signal is sinusoidal. This causes the graphs to resemble morphed $\cos^2$ functions. Fitting these curves is not trivial. It is deemed sufficient to roughly estimate the amount of phase modulation achieved by different modulation voltages. The estimated phase modulations can be seen in figure 3.5(b). According to equation (3.5) the relation between the phase modulation and the modulation voltage should be linear. Fitting the data with a linear function validates the estimation of the phase modulation. Since the fitted values are only estimations, the errors are estimated generously to be 0.15 $[2\pi]$.

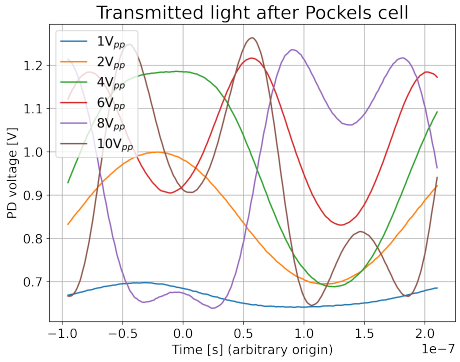

(a) Signal of the laser light transmitted by the Pockels cell while driving polarisation modulation (here effectively amplitude modulation) with the EOM.

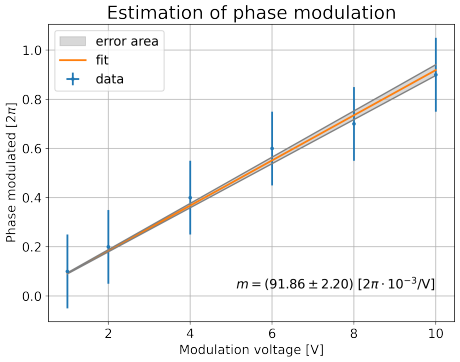

(b) Linear fit of the estimation of the phase modulation at different modulation voltages.

Figure 3.5: Transmitted light of Pockels cell and estimated phase modulations for different modulation voltages. Note that a modulation from one maximum to the next would equal 2π phase modulation. The estimated phase modulations are fitted with a linear fit function $\Delta\phi = m \cdot V$.

As mentioned in section 3.1 the quality of the error signal is dependent on the amount of phase modulation. Therefore, it is useful to have a wide range of possible phase modulation to be able to find an optimum, along with the other parameters $\phi_{s,a}$ and ω_m.

Forming of Sidebands

Using a spectrum analyzer, the pump beam sidebands created by the EOM can be observed. Figure 3.6 shows the sidebands for various modulation voltages with and without a 4.5 MHz lowpass filter to suppress sidebands of higher order.

From figure 3.6 it becomes apparent, that higher modulation voltages increases the amount of power located in the sidebands, even up to the point where the sideband of the second order (at twice the frequency) becomes visible. Three things are important to note here. Firstly, the amplitudes of the sidebands are fluctuating strongly. Therefore, one can not directly compare the amplitudes/powers measured here. Secondly, the frequency depicted here is slightly larger than the resonance frequency determined by the fit of the EOM resonance (see section 3.3.1). This is because the fit has a slight inaccuracy due to the disturbances in the resonance curve (as mentioned in section 3.3.1). This frequency was chosen to achieve the highest possible power in sidebands at a fixed modulation voltage.

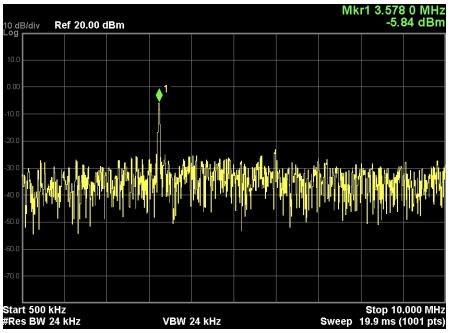

(a) Frequency sideband(s) of pump beam at $V_{\mathrm{PP,mod}} = 1\,\mathrm{V}$.

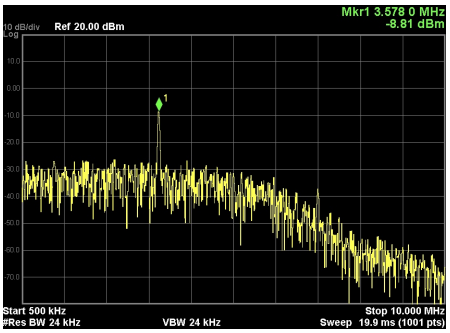

(b) Frequency sideband(s) of pump beam at $V_{\mathrm{PP,mod}} = 1\,\mathrm{V}$ with 4.5 MHz lowpass filter.

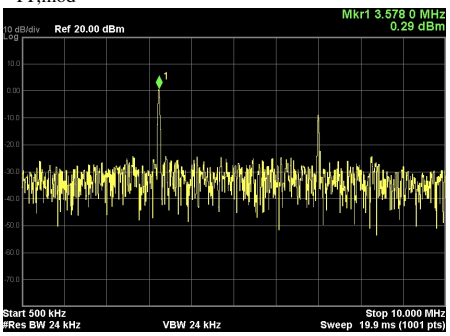

(c) Frequency sideband(s) of pump beam at $V_{\mathrm{PP,mod}} = 4\,\mathrm{V}$.

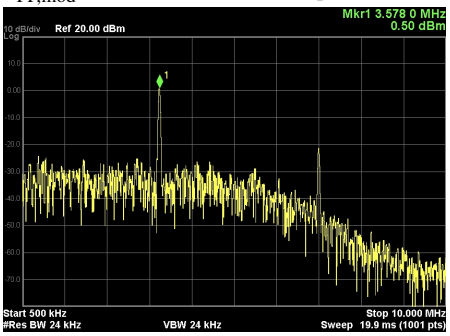

(d) Frequency sideband(s) of pump beam at $V_{\mathrm{PP,mod}} = 4\,\mathrm{V}$ with 4.5 MHz lowpass filter.

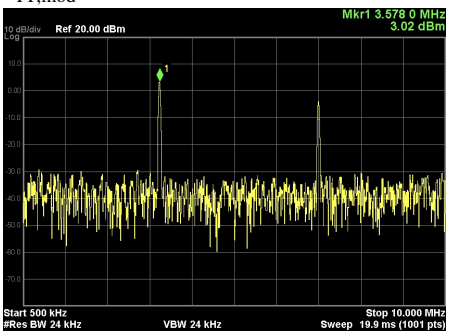

(e) Frequency sideband(s) of pump beam at $V_{\mathrm{PP,mod}} = 7\,\mathrm{V}$.

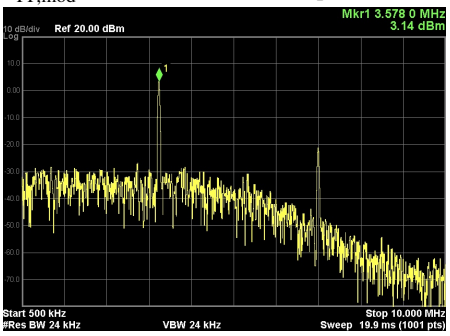

(f) Frequency sideband(s) of pump beam at $V_{\mathrm{PP,mod}} = 7\,\mathrm{V}$ with 4.5 MHz lowpass filter.

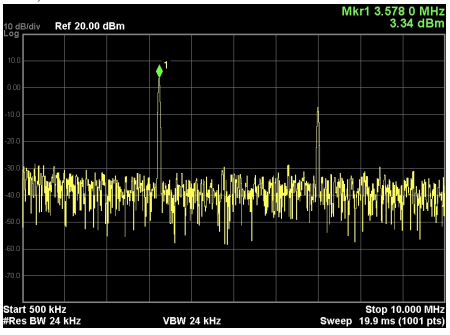

(g) Frequency sideband(s) of pump beam at $V_{\mathrm{PP,mod}} = 10\,\mathrm{V}$.

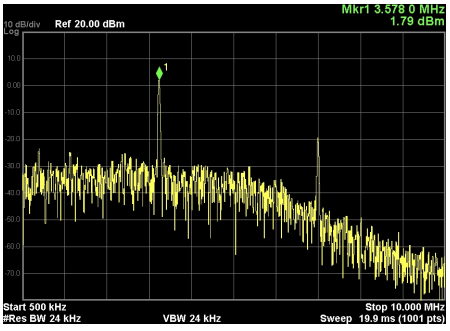

(h) Frequency sideband(s) of pump beam at $V_{\mathrm{PP,mod}} = 10\,\mathrm{V}$ with 4.5 MHz lowpass filter.

Figure 3.6: Visualization of frequency sidebands of the pump beam for various (peak to peak) modulation voltages.

Lastly, one can see the suppressing of the sideband of the second order when implementing a 4.5 MHz lowpass filter.

3.3.3 Creation of Error Signal with MTS

Using the probe beam and modulation signal one can create an error signal with the setup described in section 3.2. These error signals for the $5S_{1/2}$ ($F = 3$) to $6P_{3/2}$ ($F = 2, 3, 4$) transitions are depicted in figure 3.7 and 3.8. Despite there being three Lamb dips and three cross-over resonances, only two distinct beat notes (for the cross-over resonance of $F = 3$ and $F = 4$ (Co(3/4)) and for the Lamb dip of $F = 4$) can be observed. This might be caused by the frequency shift of the sidebands (relative to the main laser frequency) $\Delta\nu \approx 3.5\,\mathrm{MHz}$ being too large to create adequate error signals for Lamb dips/cross-over resonances that are as close to each other as the ones here. Adjusting the resonance frequency of the EOM circuit and therefore the modulation frequency ω_w might be a way to solve this issue.

The shape of the error signal can be adjusted by tuning the phase between the driving signal of the EOM and the identical second signal put into the mixer. Ideally, the beat note has a very steep monotonous slope and the highest possible amplitude (peak to peak). However, as mentioned in 3.1.2, the phases for optimizing one of these parameters respectively are not the same. Changing the phase for optimizing the slope by 180° causes the beat note slope to change from rising to falling (or vice versa). Though for stabilizing the laser to this signal, both, a falling and a rising slope, are suitable.

Another important aspect is that one can observe an increase in the beat note amplitude for increasing the modulation voltages. For higher modulation voltages the amount of power in the frequency sidebands increases. This might serve as an explanation as to why the amplitude of the beat notes increases accordingly. However, indefinitely increasing the modulation voltage should prove to be ineffective in this case. The power attributed to the sidebands of the beam is drained from the carrier frequency. Losing too much power in the carrier frequency effectively means driving the energy level transitions less which in turn has a negative influence on the overall Doppler-free spectroscopy, ultimately impairing the error signal. This line of reasoning suggests that there is an optimal modulation voltage which however might be larger than the 10 V used here. For clarification it is useful to note that a modulation of 2π is not equal to 0 here since the modulation is solely affecting the phase/frequency and not the polarization. Hence this point can not be used to explain the fact that there should be an optimal modulation voltage.

Additionally, it is important to note that for higher modulation voltages the Lamb dips and cross-over resonances change their shape and seem to merge into one another. This can be explained by the modulation of the pump beam being transferred to the probe beam. This is discussed in more detail in ref. [24].

Another thing to mention is that the high resolution mode of the oscilloscope gets rid of most of the noise on the error signal. However, the actual signal can be displayed using normal mode of the oscilloscope (see 3.8(a)). One can clearly see that the signal to noise ratio is too low for the signal to be used as a signal for frequency stabilization. The sources of noise still have to be identified.

It is also important to address that the error signal has an offset which is made visible by using DC coupling (see 3.8(b)). This offset stems from the modulation signal, put into the mixer. However, it is unclear how this purely AC signal can cause a DC offset on the error signal. Despite this, using a DC-block should be an easy solution to the problem.

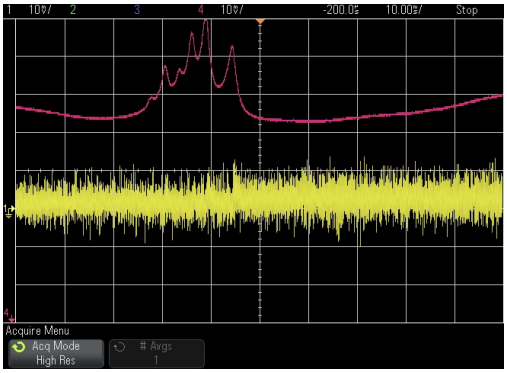

(a) Error signal (coupled AC with high resolution mode) including Lamb dips at modulation voltage $V_{PP} = 0\,V$.

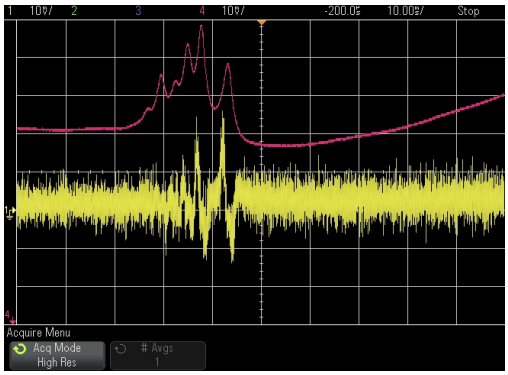

(b) Error signal (coupled AC with high resolution mode) including Lamb dips for modulation voltage $V_{PP} = 2\,V$.

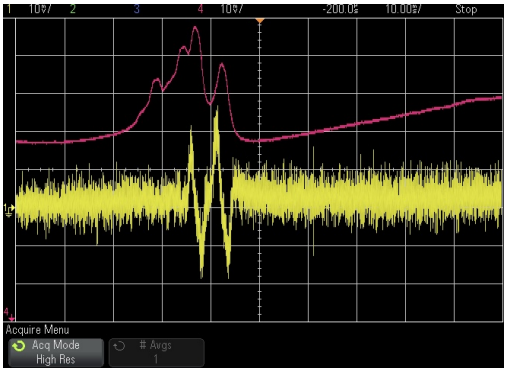

(c) Error signal (coupled AC with high resolution mode) including Lamb dips for modulation voltage $V_{PP} = 4\,V$.

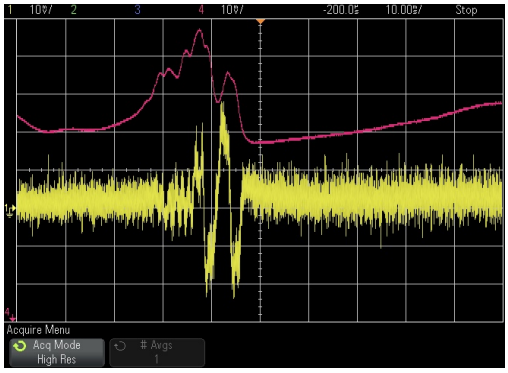

(d) Error signal (coupled AC with high resolution mode) including Lamb dips for modulation voltage $V_{PP} = 6\,V$.

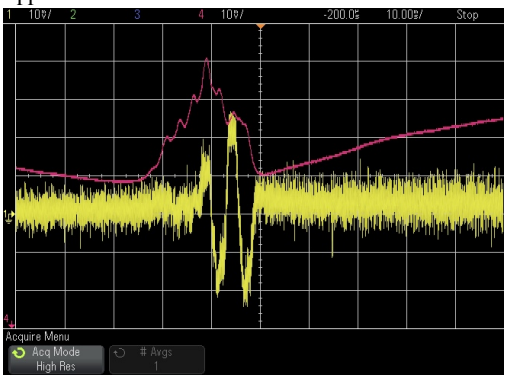

(e) Error signal (coupled AC with high resolution mode) including Lamb dips for modulation voltage $V_{PP} = 8\,V$.

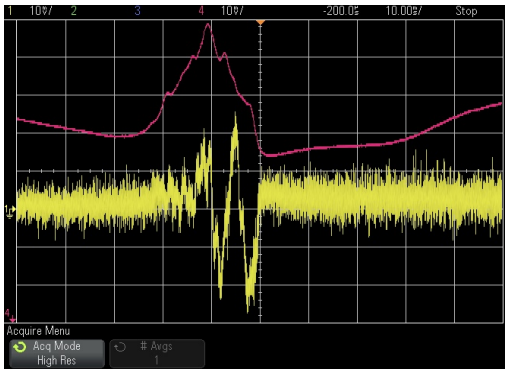

(f) Error signal (coupled AC with high resolution mode) including Lamb dips for modulation voltage $V_{PP} = 10\,V$.

Figure 3.7: Error signals and Lamb dips at different modulation voltages. High resolution mode of the oscilloscope, coupled AC.

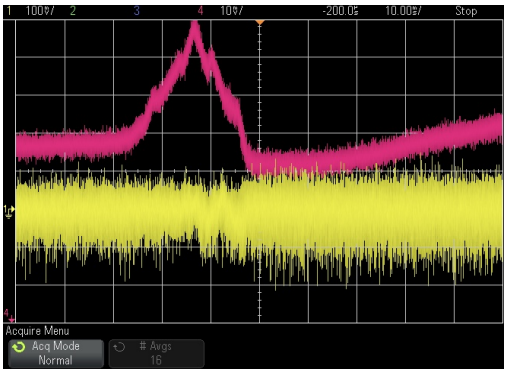

(a) Error signal (coupled AC with normal mode) including Lamb dips for modulation voltage $V_{\mathrm{PP}} = 10\,\mathrm{V}$.

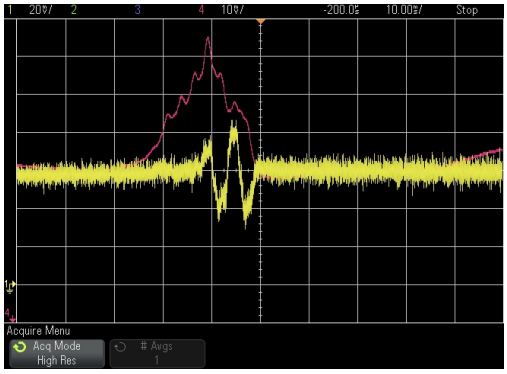

(b) Error signal (coupled DC with high resolution mode) including Lamb dips for modulation voltage $V_{\mathrm{PP}} = 8\,\mathrm{V}$.

Figure 3.8: Error signals using normal mode instead of high resolution of the oscilloscope and coupled DC instead of AC.

Due to time restraints, optimizing this error signal along with its three parameters M, ω_w and ϕ was not possible.

CHAPTER 4

Conclusion

The goal of this this thesis is to use MTS to generate an error signal for frequency-stabilizing a laser to hyperfine transitions of Rubidium.

To summarize, the **high temperature cell setup** can largely be characterized as a success, despite not being able to reach the temperature aim of 150°C. The goal was to achieve a sufficient amount of laser light absorption to increase the overall visibility of the spectrum. This is accomplished. The only issue is insufficient heating power and/or insulation. The heating setup keeps the cell windows from coating with Rubidium and enables Doppler-free spectroscopy of the $5S_{1/2} \rightarrow 6P_{3/2}$ transition as it was designed to do.

Both the **absortion spectrum** and the **saturated absorption spectrum** can be observed with their respective experimental setups. The setup allows for a clear distinction of hyperfine states. Their parameters evaluated here match the theoretically expected ones for the most part.

Regarding the **EOM** it can be said that the resonance circuit works as intended, apart from the mechanical oscillation disturbances, which, however, largely do not impair its functionality. The modulation frequency should be much lower than the width of the Lamb dips to be able to freely stabilize the laser to any hyperfine state. Therefore the modulation frequency of $\approx 3.5\,\mathrm{MHz}$ might still be too large since the modulation transferred to the pump beam seems to interfere with other Lamb dips. Despite the fact that the resonance frequency might not be optimal, the maximum phase modulation achieved $\Delta\phi_{\mathrm{max}} \lessapprox 2\pi$ is considered sufficient here. The sidebands created with said phase modulation can also be observed.

The **creation of error signals** is possible. Distinct beat notes can be observed for the $5S_{1/2}$ $(F = 3)$ to $6P_{3/2}$ $(F = 4)$ transition and the corresponding crossover resonance $(F = 3, 4)$. These error signals are also shown for different modulation voltages. However, due to time restraints, their characteristics are not quantitatively evaluated. Considering the amount of noise on the error signals, this serves more as a proof of concept than an actual laser stabilization signal, which is still a major success.

CHAPTER 5

Outlook

Despite accomplishing the creation of error signals using MTS, a lot remains to be done (or can at least be improved) to be able to use these signals to frequency-stabilize the laser.

Regarding the **high temperature cell setup** the main thing to improve is the maximum temperature which can be reached. Although the (saturated) absorption spectrum is clearly visible at 100 °C, reaching temperatures of around 150 °C should further improve the laser light absorption because of an increase of the vapor pressure [6]. This can be achieved by either increasing the overall heating power by using more heating cartridges or by improving the insulation of the cell. Simply wrapping the cell in aluminium foil causes the individual layers to be tightly stacked on top of each other at the widest part of the cell contraption (the copper blocks) impairing the insulation effectiveness. It might prove to be relatively efficient to fix this problem first, before increasing the heating power. Using a thermal camera might be helpful when dealing with this issue. Though it has to be considered that very high temperatures will lead to a possibly not insignificant amount of pressure broadening. As a consequence there should be an optimal cell temperature for this setup.

The **beam parameters** can also be optimized. Apart from finding the optimal pump and probe beam power(-ratio) it might also be worth experimenting with different beam widths in the spectroscopy cell by placing telescopes in front of each cell window. Diffusing the beam width decreases the intensity while maintaining the same net power. This allows the use of higher powers while keeping power broadening to a minimum. A side effect of a greater beam width is that the overall overlap of pump and probe beam is less sensitive to minor alignment inaccuracies.

The **EOM setup** can be improved by adjusting a number of different things. The first thing is to increase the inductivity used in the resonance circuit to achieve a smaller resonance frequency. To reduce any instability of the resonance frequency caused for example by unwanted movement of wires it seems logical to solder the entire resonance circuit directly to a small circuit board. Together with a proper housing this should largely remove any kind of instability. Improving the resonance amplitude (impedance matching) might be possible by placing an additional inductor in series with the rest of the resonance circuit. Suspending the EOM crystal capacitor between small rubber strips might help to dampen the mechanical oscillation disturbances in the resonance.

Regarding the actual **creation of the error signal** the signal-to-noise ratio is the main thing that needs improvement. After the main sources of noise are identified they need to be dealt with properly to ensure a stable and reliable laser stabilization. Also, for the three parameters of the error signal M, ω_w and ϕ a suitable combination, if not an optimum, has to be found.

Once all of these elements have been dealt with to a sufficient degree the feedback-circuit for the laser stabilization can be setup and optimized too. Then the stabilized laser can be coupled into a fiber to excite the Rb^{87} $5S_{1/2} \rightarrow 6P_{3/2}$ in another experiment.

CHAPTER 6

Acknowledgements

I would like to thank Sebastian Hofferberth for giving me the opportunity to work on this project in his research group. Thanks to the entire Nonlinear Quantum Optics group for making me feel welcome! Also, I want to thank Frank Vewinger for being the second appraiser for this thesis. I want to express my gratitude especially to Lukas Ahlheit and Nina Stiesdal for their constant guidance throughout this project. Their input and insights have been vital for the success of this experiment and I am very glad i was given the opportunity to work with them! I want to thank everyone who proofread my thesis and gave me feedback. Lastly, I want to thank my family, which has been constantly supporting me throughout this project.

Bibliography

[1] H. J. Metcalf and P. van der Straten, *Laser cooling and trapping of atoms*, J. Opt. Soc. Am. B **20** (2003) 887, URL: https://opg.optica.org/josab/abstract.cfm?URI=josab-20-5-887 (cit. on p. 1).

[2] C. Wieman and T. W. Hänsch, *Doppler-Free Laser Polarization Spectroscopy*, Phys. Rev. Lett. **36** (20 1976) 1170, URL: https://link.aps.org/doi/10.1103/PhysRevLett.36.1170 (cit. on p. 1).

[3] W. Demtröder, *Laser Spectroscopy; Vol. 2: Experimental Techniques*, 4th ed., 2008 (cit. on pp. 1, 10, 16).

[4] C. P. Pearman et al., *Polarization spectroscopy of a closed atomic transition: applications to laser frequency locking*, Journal of Physics B: Atomic, Molecular and Optical Physics **35** (2002) 5141, URL: https://dx.doi.org/10.1088/0953-4075/35/24/315 (cit. on p. 1).

[5] G. C. Bjorklund, *Frequency-modulation spectroscopy: a new method for measuring weak absorptions and dispersions*, Opt. Lett. **5** (1980) 15, URL: https://opg.optica.org/ol/abstract.cfm?URI=ol-5-1-15 (cit. on p. 1).

[6] P. C. et al., *Stabilizing diode laser to 1 Hz-level Allan deviation with atomic spectroscopy for Rb four-level active optical frequency standard*, Applied Physics B, Lasers and Optics **125** (2019), URL: https://doi.org/10.1007/s00340-019-7313-x (cit. on pp. 1, 4, 33).

[7] J. Lampen, H. Nguyen, L. Li, P. R. Berman, and A. Kuzmich, *Long-lived coherence between ground and Rydberg levels in a magic-wavelength lattice*, Phys. Rev. A **98** (3 2018) 033411, URL: https://link.aps.org/doi/10.1103/PhysRevA.98.033411 (cit. on p. 1).

[8] D. R. L. (Ed.), *CRC Handbook of Chemistry and Physics*, 81st ed., CRC Press, Boca Raton, 2000 (cit. on p. 3).

[9] K. J. R. Rosman and P. D. P. Taylor, *Isotopic compositions of the elements 1977 (Technical Report)*, Pure and Applied Chemistry **70** (1998) 224, URL: https://doi.org/10.1351/pac199870010217 (visited on 01/29/2024) (cit. on p. 3).

[10] C. G. et al., *Absolute frequency measurement of rubidium 5S-6P transitions*, PHYSICAL REVIEW A 102, 012804 (2020) (cit. on pp. 4, 14, 16, 44).

[11] S. Millman and M. Fox, *Nuclear Spins and Magnetic Moments of Rb^{85} and Rb^{87}*, PHYSICAL REVIEW **50** (1936) 225 (cit. on p. 3).

[12] W. C. Martin and W. L. Wiese, *Atomic Spectroscopy*, National Institute of Standards and Technology, Gaithersburg, Maryland 20899 18, URL: https://www.nist.gov/pml/atomic-spectroscopy-compendium-basic-ideas-notation-data-and-formulas (visited on 01/29/2024) (cit. on p. 3).

[13] C. D. Herold et al., *Precision Measurement of Transition Matrix Elements via Light Shift Cancellation*, Phys. Rev. Lett. **109** (24 2012) 243003, URL: https://link.aps.org/doi/10.1103/PhysRevLett.109.243003 (cit. on p. 4).

[14] D. A. Steck, *Rubidium 87 D Line Data*, (2001) (cit. on p. 4).

[15] A. V. et al., *Enhanced frequency up-conversion in RB vapor*, Optics express **18** (2010) 17020 (cit. on p. 4).

[16] S. Z. et al., *Compact Rb optical frequency standard with 10^{-15} stability.*, Review of Scientific Instruemnts **88** (2017) 103016 (cit. on p. 4).

[17] R. Nave, *Stefan-Boltzmann law*, URL: http://hyperphysics.phy-astr.gsu.edu/hbase/thermo/stefan.html (visited on 01/30/2024) (cit. on p. 5).

[18] O. Marti, *Strahlungsgesetze*, URL: http://wwwex.physik.uni-ulm.de/lehre/ap-2019/ap-2019se9.html (visited on 03/02/2024) (cit. on p. 5).

[19] T. U. Braunschweig, *Line Width and Line Shape*, URL: http://www.pci.tu-bs.de/aggericke/PC4e/Kap_III/Linienbreite.htm (visited on 02/24/2024) (cit. on pp. 6, 10).

[20] A. Akimov et al., *Study of the Rabi splitting at the 5P3/2 $\rightarrow$ 5D5/2,3/2 transitions in the 87Rb atom upon cascade excitation in a magnetooptical trap*, Quantum Electronics **40** (2010) 139 (cit. on p. 9).

[21] A. Vernier, S. Franke-Arnold, E. Riis, and A. S. Arnold, *Enhanced frequency up-conversion in Rb vapor*, Opt. Express **18** (2010) 17020, URL: https://opg.optica.org/oe/abstract.cfm?URI=oe-18-16-17020 (cit. on p. 10).

[22] R. Paschotta, *Pockels Effect*, RP Photonics Encyclopedia, 2005, URL: https://www.rp-photonics.com/pockels_effect.html (visited on 02/26/2024) (cit. on p. 19).

[23] P. Y. Amnon Yariv, *Optical Waves in Crystals - Propagation and Control of Laser Radiation*, John Wiley and Sons, 1983 (cit. on pp. 19, 20).

[24] T. P. et al., *Optimization strategies for modulation transfer spectroscopy applied to laser stabilization*, Optics Express **26** (2018) (cit. on pp. 20, 21, 28).

[25] R. K. Raj, D. Bloch, J. J. Snyder, G. Camy, and M. Ducloy, *High-Frequency Optically Heterodyned Saturation Spectroscopy Via Resonant Degenerate Four-Wave Mixing*, Phys. Rev. Lett. **44** (19 1980) 1251, URL: https://link.aps.org/doi/10.1103/PhysRevLett.44.1251 (cit. on p. 21).

[26] E. Hecht, *Optics: International Edition*, 4th ed., 2003 (cit. on p. 22).

[27] M. O. A. W. Warner and G. A. Coquin, *Determination of Elastic and Piezoelectric Constants for Crystals in Class(3m)*, (1966) (cit. on p. 24).

APPENDIX A

Appendix

A.1 Figures

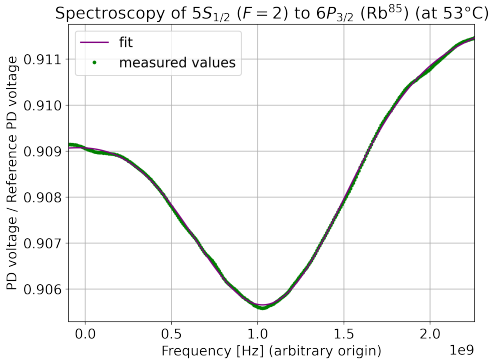

(a) Fitted absorption spectrum of the Rb^{85} $5S_{1/2}$ ($F = 2$) to $6P_{3/2}$ transition at 53 °C.

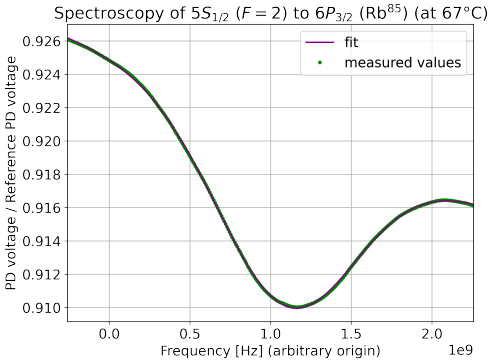

(b) Fitted absorption spectrum of the Rb^{85} $5S_{1/2}$ ($F = 2$) to $6P_{3/2}$ transition at 67 °C.

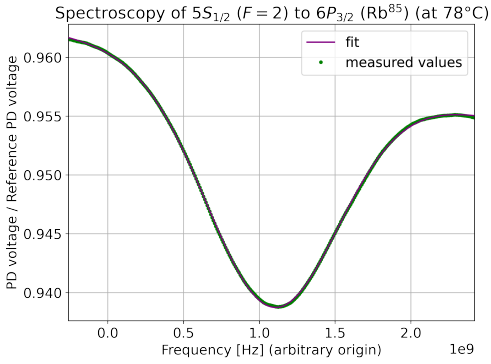

(c) Fitted absorption spectrum of the Rb^{85} $5S_{1/2}$ ($F = 2$) to $6P_{3/2}$ transition at 78 °C.

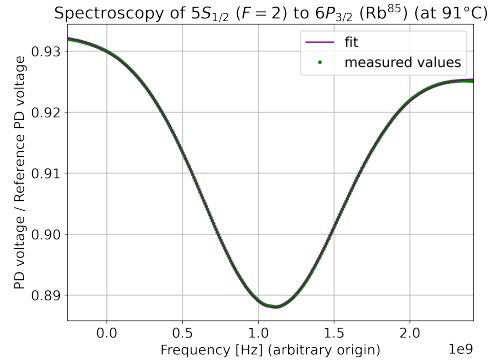

(d) Fitted absorption spectrum of the Rb^{85} $5S_{1/2}$ ($F = 2$) to $6P_{3/2}$ transition at 91 °C.

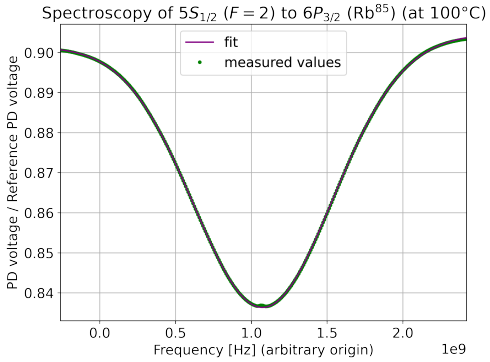

(e) Fitted absorption spectrum of the Rb^{85} $5S_{1/2}$ ($F = 2$) to $6P_{3/2}$ transition at 100 °C.

Figure A.1: Fitted absorption spectra of the Rb^{85} $5S_{1/2}$ ($F = 2$) to $6P_{3/2}$ transition at different temperatures.

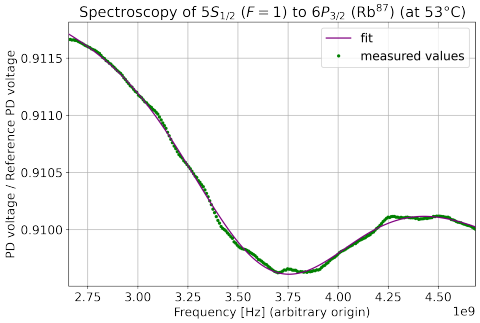

(a) Fitted absorption spectrum of the Rb^{87} $5S_{1/2}$ ($F = 1$) to $6P_{3/2}$ transition at 53 °C.

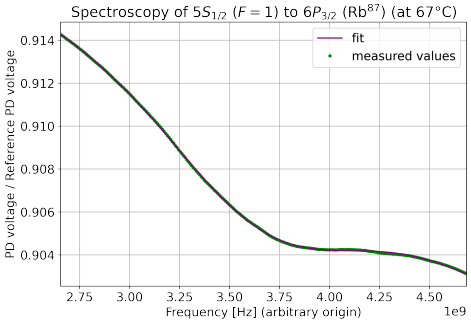

(b) Fitted absorption spectrum of the Rb^{87} $5S_{1/2}$ ($F = 1$) to $6P_{3/2}$ transition at 67 °C.

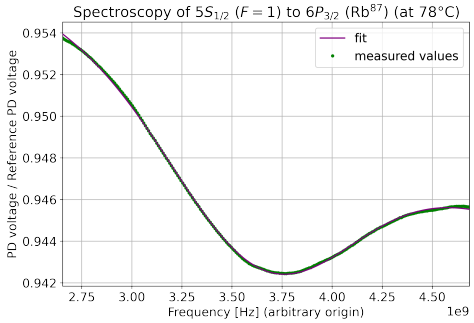

(c) Fitted absorption spectrum of the Rb^{87} $5S_{1/2}$ ($F = 1$) to $6P_{3/2}$ transition at 78 °C.

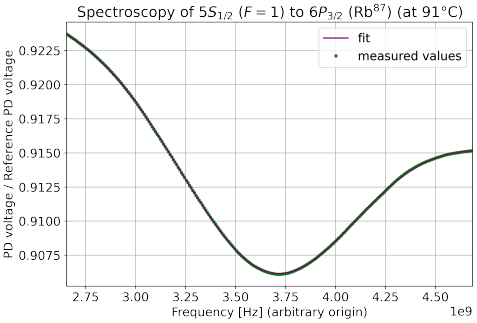

(d) Fitted absorption spectrum of the Rb^{87} $5S_{1/2}$ ($F = 1$) to $6P_{3/2}$ transition at 91 °C.

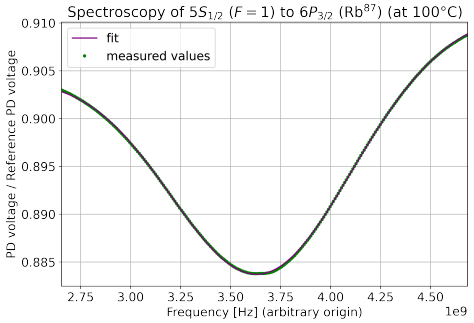

(e) Fitted absorption spectrum of the Rb^{87} $5S_{1/2}$ ($F = 1$) to $6P_{3/2}$ transition at 100 °C.

Figure A.2: Fitted absorption spectra of the Rb^{87} $5S_{1/2}$ ($F = 1$)) to $6P_{3/2}$ transition at different temperatures.

A.2 Tables

Isotope	Initial state F	Transition frequency[THz]	Frequency offset [MHz]
Rb^{87}	2	713.281677050	-1173.054
Rb^{85}	3	713.282850104	0
Rb^{85}	2	713.285885834	3035.730
Rb^{87}	1	713.288511730	5661.626

Table A.1: Possible transitions in Rb^{85} and Rb^{87} ($5S_{1/2} \rightarrow 6P_{3/2}$) considering hyperfine splitting for ground state only [10]. Frequency offset relative to $5S_{1/2}(F = 3) \rightarrow 6P_{3/2}$.

Transition	Amplitude a [10^{-3}]	Offset c [ms]	Width h [ms]
Rb^{87} $5S_{1/2}$ ($F = 2$) to $6P_{3/2}$	(-46.47 ± 0.06)	(-39.60 ± 0.02)	(7.622 ± 0.019)
Rb^{85} $5S_{1/2}$ ($F = 3$) to $6P_{3/2}$	(-101.3 ± 0.1)	(-24.46 ± 0.01)	(6.888 ± 0.007)
Rb^{85} $5S_{1/2}$ ($F = 2$) to $6P_{3/2}$	(-67.11 ± 0.05)	(13.36 ± 0.01)	(6.717 ± 0.007)
Rb^{87} $5S_{1/2}$ ($F = 1$) to $6P_{3/2}$	(-24.14 ± 0.06)	(44.85 ± 0.02)	(6.684 ± 0.021)

Table A.2: Fit parameters of Rubidium transitions at 100°C. Note: Slope $m = (0.138 \pm 0.001)$ 1/s and Slope offset $b = (0.902 \pm 0.001)$. The fit is depicted in figure 2.6(c).

Transition	Amplitude a [10^{-3}]	Offset c [GHz]	Width h [MHz]
Rb^{87} $5S_{1/2}$ ($F = 2$) to $6P_{3/2}$	(-46.47 ± 0.06)	(-3.205 ± 0.002)	(616.9 ± 1.5)
Rb^{85} $5S_{1/2}$ ($F = 3$) to $6P_{3/2}$	(-101.3 ± 0.1)	(-1.979 ± 0.001)	(557.4 ± 0.6)
Rb^{85} $5S_{1/2}$ ($F = 2$) to $6P_{3/2}$	(-67.11 ± 0.05)	(1.082 ± 0.001)	(543.6 ± 0.5)
Rb^{87} $5S_{1/2}$ ($F = 1$) to $6P_{3/2}$	(-24.14 ± 0.06)	(3.630 ± 0.001)	(540.9 ± 1.7)

Table A.3: Fit parameters of calibrated Rubidium transitions at 100°C. Note: Slope $m = (1.707 \pm 0.009)$ 1/THz and Slope offset $b = (0.902 \pm 0.001)$. The fit is depicted in figure 2.6(d).

Temp. [°C]	Amplitude a [-10^{-3}]	Offset c [GHz]	Width h [MHz]	Slope m [1/THz]	Slope Offset b
53	(4.688 ± 0.008)	(1.069 ± 0.001)	(506.9 ± 1.2)	(1.011 ± 0.005)	(0.909 ± 0.001)
67	(10.91 ± 0.01)	(1.093 ± 0.001)	(503.5 ± 0.7)	(−3.889 ± 0.006)	(0.925 ± 0.001)
78	(19.74 ± 0.01)	(1.084 ± 0.001)	(509.1 ± 0.4)	(−2.473 ± 0.006)	(0.961 ± 0.001)
91	(41.24 ± 0.02)	(1.089 ± 0.001)	(525.6 ± 0.3)	(−2.524 ± 0.008)	(0.932 ± 0.001)
100	(66.75 ± 0.02)	(1.077 ± 0.001)	(539.3 ± 0.3)	(1.117 ± 0.010)	(0.902 ± 0.001)

Table A.4: Fit parameters of the Rb^{85} $5S_{1/2}$ ($F = 2$) to $6P_{3/2}$ transition at different temperatures. The fits are depicted in figure A.1.

Temp. [°C]	Amplitude a [-10^{-3}]	Offset c [GHz]	Width h [MHz]	Slope m [1/THz]	Slope Offset b
53	(1.259 ± 0.005)	(3.660 ± 0.002)	(439.5 ± 2.5)	(−0.833 ± 0.004)	(0.914 ± 0.001)
67	(3.860 ± 0.009)	(3.674 ± 0.001)	(509.6 ± 1.5)	(−5.505 ± 0.006)	(0.929 ± 0.001)
78	(7.776 ± 0.002)	(3.650 ± 0.001)	(527.5 ± 1.5)	(−4.204 ± 0.010)	(0.966 ± 0.001)
91	(14.14 ± 0.01)	(3.660 ± 0.001)	(513.0 ± 0.5)	(−4.263 ± 0.007)	(0.936 ± 0.001)
100	(23.93 ± 0.01)	(3.654 ± 0.001)	(530.40 ± 0.06)	(2.818 ± 0.012)	(0.897 ± 0.001)

Table A.5: Fit parameters of the Rb^{87} $5S_{1/2}$ ($F = 1$) to $6P_{3/2}$ transition at different temperatures. The fits are depicted in figure A.2.

Peak	Amplitude a [$10^{-29}\mathrm{Hz}^4$]	Offset c [MHz]	Width h [MHz]
$F = 1$	(0.127 ± 0.028)	(−276.0 ± 0.2)	(4.862 ± 0.584)
Co1/2	(1.269 ± 0.037)	(−251.3 ± 0.1)	(6.912 ± 0.111)
$F = 2$	(1.184 ± 0.043)	(−226.5 ± 0.1)	(8.538 ± 0.166)
Co1/3	(1.813 ± 0.029)	(−209.0 ± 0.1)	(7.772 ± 0.071)
Co2/3	(4.085 ± 0.033)	(−184.0 ± 0.1)	(9.771 ± 0.044)
$F = 3$	(2.290 ± 0.029)	(−141.7 ± 0.1)	(11.04 ± 0.08)

Table A.6: Fit parameters for Rb^{87} $5S_{1/2}$ ($F = 2$) to $6P_{3/2}$ ($F = 1, 2, 3$) transition lamb dips and cross-over resonances. Note: $m = (-4.567 \pm 0.019)\,\mathrm{e} - 101/Hz$ and $b = (11.82 \pm 0.01)$. The fit is depicted in figure 2.13(c).

Peak	Amplitude A [10^{-3}]	FWHM [MHz]	Frequency difference to next peak [MHz]
$F = 1$	(7.026 ± 2.274)	(4.863 ± 0.584)	(24.73 ± 0.17)
Co1/2	(42.08 ± 1.80)	(6.913 ± 0.111)	(24.75 ± 0.06)
$F = 2$	(31.66 ± 1.63)	(8.540 ± 0.166)	(17.52 ± 0.06)
Co1/3	(67.71 ± 1.66)	(7.773 ± 0.071)	(24.95 ± 0.03)
Co2/3	(126.3 ± 1.6)	(9.775 ± 0.044)	(42.34 ± 0.03)
$F = 3$	(93.71 ± 1.73)	(11.04 ± 0.08)	

Table A.7: Calculated characteristics of the lamb dips and crossover resonances for the Rb^{87} $5S_{1/2}$ ($F = 2$) to $6P_{3/2}$ ($F = 1, 2, 3$) transitions using the fit parameters. The fit is depicted in figure 2.13(c).

Peak	Amplitude a [10^{-29}Hz^4]	Offset c [MHz]	Width h [MHz]
$F = 2$	(1.132 ± 0.077)	(-202.8 ± 0.1)	(9.134 ± 0.330)
Co2/3	(3.407 ± 0.099)	(-192.8 ± 0.1)	(8.515 ± 0.110)
$F = 3$	(3.194 ± 0.183)	(-182.6 ± 0.1)	(10.12 ± 0.22)
Co2/4	(3.837 ± 0.086)	(-173.6 ± 0.1)	(8.207 ± 0.078)
Co3/4	(7.645 ± 0.061)	(-163.5 ± 0.1)	(10.12 ± 0.04)
$F = 4$	(4.687 ± 0.034)	(-144.8 ± 0.1)	(10.71 ± 0.05)

Table A.8: Fit parameters for Rb^{85} $5S_{1/2}$ ($F = 3$) to $6P_{3/2}$ ($F = 2, 3, 4$) transition lamb dips and cross-over resonances. Note: $m = (-1.828 \pm 0.042) \times 10^{-10}$ 1/Hz and $b = (10.96 \pm 0.01)$. The fit is depicted in figure 2.13(f).

Peak	Amplitude A [10^{-3}]	FWHM [MHz]	Frequency difference to next peak [MHz]
$F = 2$	(32.98 ± 3.51)	(9.136 ± 0.330)	(10.06 ± 0.09)
Co2/3	(126.4 ± 5.0)	(8.517 ± 0.110)	(10.17 ± 0.05)
$F = 3$	(93.57 ± 5.99)	(10.120 ± 0.213)	(8.962 ± 0.043)
Co2/4	(188.9 ± 5.6)	(8.209 ± 0.078)	(10.19 ± 0.02)
Co3/4	(279.5 ± 3.1)	(10.120 ± 0.038)	(18.62 ± 0.02)
$F = 4$	(194.9 ± 2.1)	(10.720 ± 0.041)	

Table A.9: Calculated characteristics of the lamb dips and crossover resonances for the Rb^{85} $5S_{1/2}$ ($F = 3$) to $6P_{3/2}$ ($F = 2, 3, 4$) transitions using the fit parameters. The fit is depicted in figure 2.13(f).

Peak	Amplitude a [10^{-29}Hz^4]	Offset c [MHz]	Width h [MHz]
$F = 0$	(0.011 ± 0.007)	(-262.4 ± 0.3)	(2.843 ± 0.895)
Co0/1	(2.608 ± 0.086)	(-242.0 ± 0.1)	(10.19 ± 0.14)
$F = 1$	(3.806 ± 0.222)	(-230.1 ± 0.1)	(15.09 ± 0.40)
Co0/2	(1.497 ± 0.068)	(-216.2 ± 0.1)	(9.473 ± 0.189)
Co1/2	(4.945 ± 0.065)	(-204.1 ± 0.1)	(12.86 ± 0.08)
$F = 2$	(2.569 ± 0.045)	(-178.3 ± 0.1)	(13.92 ± 0.19)

Table A.10: Fit parameters for Rb^{87} $5S_{1/2}$ ($F = 1$) to $6P_{3/2}$ ($F = 0, 1, 2$) transition lamb dips and cross-over resonances. Note: $m = (-8.795 \pm 0.169) \times 10^{-11}$ 1/Hz and $b = (12.23 \pm 0.01)$. The fit is depicted in figure 2.13(k).

Peak	Amplitude A [10^{-3}]	FWHM [MHz]	Frequency difference to next peak [MHz]
$F = 0$	(1.942 ± 1.634)	(2.843 ± 0.895)	(20.42 ± 0.14)
Co0/1	(42.94 ± 1.83)	(10.19 ± 0.14)	(11.80 ± 0.09)
$F = 1$	(31.53 ± 2.47)	(15.100 ± 0.396)	(14.01 ± 0.09)
Co0/2	(35.70 ± 2.16)	(9.475 ± 0.190)	(12.08 ± 0.05)
Co1/2	(71.78 ± 1.30)	(12.870 ± 0.081)	(25.75 ± 0.04)
$F = 2$	(41.69 ± 1.07)	(13.930 ± 0.121)	

Table A.11: Calculated characteristics of the lamb dips and crossover resonances for the Rb^{87} $5S_{1/2}$ ($F = 1$) to $6P_{3/2}$ ($F = 0, 1, 2$) transitions using the fit parameters. The fit is depicted in figure 2.13(k).

a [dBm/Hz^4]	b [dBm]	c [GHz]	h [kHz]	A [dBm]	$\Delta\nu_{FWHM}$ [kHz]
$(-4.536 \pm 0.083) \times 10^{23}$	(-19.26 ± 0.01)	(3.533 ± 0.001)	(97.07 ± 1.03)	(-3.86 ± 0.11)	(97.1 ± 1.0)

Table A.12: Fit parameters of the EOM resonance fit. The fit is depicted in figure 3.4(c).

List of Figures

List of Tables